


OPEN ACCESS
EDITED BY

Andrea Paoletta,
 University of Modena and Reggio
 Emilia, Italy

REVIEWED BY

Ntalane Sello Seroka,
 Council for Scientific and Industrial
 Research (CSIR), South Africa
 Yu-Lin Bai,
 Taiyuan University of Technology, China

***CORRESPONDENCE**

Georg Garnweitner,
 ✉ g.garnweitner@tu-braunschweig.de

RECEIVED 30 November 2025

REVISED 06 February 2026

ACCEPTED 23 February 2026

PUBLISHED 30 March 2026

CITATION

Kilonzi F, Jagau R, Hashemi P,
 Jean-Fulcrand A and Garnweitner G
 (2026) Green method for the synthesis
 of biobased carbon from *miscanthus* ×
giganteus for lithium-ion batteries.
Front. Energy Res. 14:1757714.
 doi: 10.3389/fenrg.2026.1757714

COPYRIGHT

© 2026 Kilonzi, Jagau, Hashemi,
 Jean-Fulcrand and Garnweitner. This is
 an open-access article distributed
 under the terms of the [Creative
 Commons Attribution License \(CC BY\)](https://creativecommons.org/licenses/by/4.0/).
 The use, distribution or reproduction in
 other forums is permitted, provided the
 original author(s) and the copyright
 owner(s) are credited and that the
 original publication in this journal is
 cited, in accordance with accepted
 academic practice. No use, distribution
 or reproduction is permitted which
 does not comply with these terms.

Green method for the synthesis of biobased carbon from *miscanthus* × *giganteus* for lithium-ion batteries

Fabisch Kilonzi^{1,2,3}, Rene Jagau^{1,2}, Payam Hashemi^{1,2},
 Annelise Jean-Fulcrand^{1,2,4} and Georg Garnweitner^{1,2*}

¹Institute for Particle Technology, Technische Universität Braunschweig, Braunschweig, Germany, ²Battery LabFactory Braunschweig (BLB), Technische Universität Braunschweig, Braunschweig, Germany, ³Department of Chemical and Process Engineering, The Technical University of Kenya, Nairobi, Kenya, ⁴General Education Department, École de Technologie Supérieure, Montréal, QC, Canada

Graphite, widely used in lithium-ion batteries (LIBs) due to its cycle stability and high conductivity, is limited by a capacity of 372 mA h g⁻¹ and its high reactivity with electrolyte components. As an alternative, nanostructured carbon materials like mesoporous carbon offer higher capacities due to their porous structures, which facilitate rapid ion transport and diffusion. This study introduces a sustainable and scalable synthesis method for bio-based mesoporous carbon derived from *miscanthus* × *giganteus* (MG), a fast-growing energy crop. Using cascaded hydrothermal carbonization followed by calcination, we produced mesoporous carbon with specific surface areas exceeding 450 m² g⁻¹, substantially higher than the 20–80 m² g⁻¹ of the original hydrochar. This approach avoids the chemical waste and high costs associated with traditional pyrolysis and chemical activation methods. The resulting material achieved discharge capacities of 700 mA h g⁻¹ at 0.5 °C, outperforming commercial graphite and other chemically activated carbons from similar biomass sources with even higher specific surface area.

KEYWORDS

biochar, calcination, calcined hydrochar, hydrochar, hydrothermal carbonization, anode material

1 Introduction

Lithium-ion batteries (LIBs) have widespread applications in portable electronic devices and electric vehicles due to their advantages of high energy density and long cycle life (Zhao et al., 2020). Graphite is the most widely used anode material in LIBs due to its excellent cycle stability and electrical conductivity, but it suffers from a limited capacity of only 372 mA h g⁻¹, poor rate performance, is difficult to recycle and hence insufficient for high-energy demands and long-range electric vehicles (Zhou et al., 2019; Li et al., 2023). Therefore, there is a need for new anode active materials for high-performance electrodes to be developed. The battery grade graphite currently used in LIBs is a mixture of natural graphite (mined from geographically constrained natural deposits followed by purification using a series of energy and chemical-intensive processes) and artificial graphite which is produced from sulfur-containing petroleum residues as feedstock with a low rate of production under intensive use of fossil energy and high CO₂ emissions (Sagues et al., 2020). Graphite suffers from the formation and growth of the solid electrolyte interphase (SEI), whereby lithium

ions are consumed (leading to irreversible capacity losses) and organic components of the electrolyte are being reduced, lithium fluoride (LiF) is deposited on the graphite surface as well as gases such as C_2H_6 , C_2H_4 , CO_2 , or hydrogen fluoride (HF) are formed, all of which negatively affect the battery performance (Agubra and Fergus 2014). It has been reported that during this process, the potential cell capacity decreases in the range between 18% and 40% (Libich et al., 2017). Although prelithiation of graphite has been investigated, still irreversible capacity loss was observed (Libich et al., 2017). It is proposed that the use of hard carbons can eliminate this negative effect of the SEI layer formation, because some of these bio-based carbons have even shown increasing discharge capacities over the course of cycling, which has been interpreted as blocked pathways opening during repeated cycling (Campbell et al., 2015; Luna-Lama et al., 2022). Additionally, these bio-based carbons have attracted intense interest due to their good electrical conductivity, adjustable porosity and morphology, excellent stability as well as synergetic functional groups or self-doping with nitrogen and oxygen species after carbonization which directly translates to discharge capacities higher than graphite (Feng et al., 2020). Processing of these bio-based carbons is also easy compared to graphite functionalization for achieving higher discharge capacities (Deng et al., 2016; Al Rai and Yanilmaz 2021). For all carbon materials such as carbon nanotubes, graphene, or mesoporous carbon, high conductivity and specific surface area facilitate ion diffusion and lower electrical resistance (Al Rai and Yanilmaz 2021), leading to excellent electrochemical performance. It is worthwhile to mention that soft and hard carbonaceous materials also possess high lithium-ion storage capacity. Porous hard carbons have an advantage of non-directional Li pathways to the active material, which can lead to a better resistance to overcharge compared to graphite, and are compatible with the usual electrolyte components (Zhao et al., 2016; Wang et al., 2021).

Several synthesis routes are used to synthesize porous structures in carbon, which include pyrolysis, hydrothermal carbonization, activation (Dou et al., 2019), template-based methods (Gao et al., 2014) and organic gel carbonization (Zhao et al., 2020). Pyrolysis is the most widely used method, but the process requires high temperatures, which negatively affect the porosity and the specific surface area of the resulting porous carbons. Alternatively, hydrothermal carbonization (HTC), an exothermic process which dates back to the twelfth century (Mumme et al., 2011; Funke and Ziegler 2010), seems to be a promising way to produce these porous carbons because of the mild reaction conditions, high yield, the possible use of wet biomass, short reaction time, and the formation of soluble materials as byproducts. The hydrothermal carbonization process begins with hydrolysis, which involves the breakdown of biopolymers like cellulose, hemicellulose and lignin into smaller molecules such as monosaccharides, acids, and furans. These intermediates then undergo dehydration, eliminating hydroxyl groups to form carbonyl and furan derivatives. Decarboxylation and deamination follow, releasing CO_2 and NH_3 gases and producing reactive oxygenated intermediates. These species polymerize and aromatize, forming a carbonaceous network with higher carbon content. The resulting hydrochar retains oxygen-containing functionalities, including carboxyl, hydroxyl, and carbonyl groups on the surface, and possesses a higher aromatization degree than

the original biomass, making it a good candidate for energy storage (Gu et al., 2015; Li et al., 2016; Yu et al., 2015).

Hydrothermal carbons (HC), commonly classified as hard carbons, are actually synthesized using renewable carbon precursor sources in an easy, cost-effective process. A wide range of natural carbon-rich organic materials such as such as jute fibers, bamboo wood (Gu et al., 2015), bamboo char (Li et al., 2016; Tian et al., 2020), microalgae (Ru et al., 2016), rice husk (Ding et al., 2013; Wang et al., 2013), sisal fibers (Yu et al., 2015), reed flowers (Zhao et al., 2020) and peanut skin have been used as natural sources of HC for LIBs. Typically, after hydrothermal carbonization, the HC is usually chemically activated to obtain high-surface-area porous activated carbon. Chemical activation is mostly favored because it is simple and economically viable as it leads to products with higher density and larger specific surface area compared to products from physical activation (Ding et al., 2013). However, the use of chemical activation increases the cost of the process, in particular because extensive washing of the final product is required which leads to a large amount of wastes. Although chemically activated carbons synthesized through cascaded pyrolysis-chemical activation have shown good electrochemical performance, non-activated carbons (hereby referred to as calcined hydrochar) equally shows good electrochemical performance in LIBs.

This investigation is focused on the synthesis and electrochemical evaluation of a mesoporous calcined hydrochar derived from *Miscanthus × giganteus* for application as an anode material in LIBs. The synthesis protocol employed an HTC step, followed by a multi-step calcination designed to induce significant pore network formation. A systematic optimization of HTC parameters (reaction time and temperature) was conducted to elucidate their influence on the structural and morphological characteristics of the intermediate hydrochar. The electrochemical performance of this hydrochar was compared to that of the hydrochar after calcination, and to a biochar synthesized via a conventional pyrolysis route. While numerous biomass-derived materials have demonstrated promising electrochemical performance as LIB anodes, their widespread application is often hindered by limitations in scalability and feedstock consistency (Chen et al., 2016; Chen et al., 2014). *Miscanthus* solves this problem because it can be readily collected in large areas and in relatively uniform quality, and is a non-edible biomass source so it does not compete with food sources. Mihajlović et al. (2018) investigated the synthesis of miscanthus hydrochar for use as solid fuel in the temperature range 180 °C–220 °C and found out that 220 °C was the optimal reaction temperature. At a 1C rate, miscanthus delivered an initial discharge capacity of 529 mA h/g, retaining 248 mA h/g after 200 cycles (Lim et al., 2020). This study presents a chemical-free, low-energy hydrothermal carbonization–multistep calcination strategy for fabricating sustainable bio-based anodes for lithium-ion batteries. By eliminating energy-intensive pyrolysis and chemical activation steps, the approach avoids the generation of hazardous chemical wastes that threaten environmental sustainability, while simultaneously delivering stable cycling, high specific capacity, and fundamental structure–property insights that provide a scalable design framework for next-generation lithium-ion and broader electrochemical energy-storage systems. To the best of our knowledge, this green synthesis strategy has not been previously

explored for the preparation of miscanthus-derived LIB active materials.

2 Materials and methods

Miscanthus × giganteus (MG): was supplied by Landwirtschaftsbetrieb Wiedermann, Lampertswalde, Germany. Technical ethanol from BERKEL AHK and isopropanol from CVH Chemie-Vertrieb Hannover were used as supplied. Distilled water (purity 0.055 μS), carboxymethyl cellulose (CMC) from Dupont (TEXTURECEL DRT 2000 PA 09), styrene-butadiene rubber (SBR) (emulsifier with 40 wt.% of solids content; BM451-B, Zeon Corporation) and carbon black (C-ENERGY™, Super C65 from Imerys SA) were used. All chemicals, analytical grade or higher in purity, were used as received without further alteration.

2.1 Material preparation

The as-received MG biomass was shredded in a blender followed by sieving at different mesh sizes to obtain three powder fractions in the range of < 180 μm. The shredded sample was then washed thoroughly with deionized water, dried at 100 °C for 12 h, and then stored in airtight containers for further experiments. The full process chain of the MG biomass-based electrode materials fabrication is schematically shown in Figure 1.

2.2 Hydrothermal carbonization and calcination

1.8 g of ground, washed and dried MG powder with a particle size less than 180 μm was first dispersed into 18 mL of distilled water in a 20 mL glass vial, magnetically stirred for 12 h and then transferred into a 45 mL PTFE cup which was fitted into a steel autoclave system from PARR Instrument Company (USA). For a thorough investigation of the hydrothermal process, the reaction time at the target temperature ranged between 18 and 120 h and the reaction temperature was varied from 200, 230, 250–260 °C. 200 °C was selected as the lowest reaction temperature because hemicellulose hydrolyzes at around 180 °C, with the major reaction part at around 200 °C, whilst cellulose does not hydrolyze below 220 °C (Mumme et al., 2011; Wang et al., 2013). For optimization of the precursor concentration, the reaction temperature was fixed at 230 °C and the reaction time of 48 h and the solid: solvent ratio varied from 1:10, 1:15 to 1:20. However, for the reported data, the optimal solid: solvent ratio of 1:10 was used. In all these experiments, after the reaction, the autoclave was cooled down to room temperature. The obtained black solid powder was then separated from the remaining aqueous solution by centrifugation (6500 rpm for 20 min) on a Hettich Universal 320 centrifuge once using water and twice with ethanol as solvent, and then dried at 80 °C in a vacuum oven for 12 h. The yield of the obtained hydrochar was in the range of 45%–48%.

The hydrochar was subjected to a controlled multi-step calcination process within a tubular furnace (Carbolite Gero, Neuhausen, Germany) under a continuous nitrogen flow of 14 mL min⁻¹ to maintain an inert atmosphere. The procedure comprised sequential thermal treatments: an initial ramp to 120 °C with an

isothermal hold for 1 h; subsequent heating to 450 °C followed by an isothermal dwell for 30 min; then elevating to 650 °C with a 30-min isothermal stage; and a final heating to 800 °C, maintained for 2 h. The entire process was conducted at a uniform heating rate of 5 °C·min⁻¹. This multi-stage calcination protocol from literature had been used to optimize the carbon content, while promoting the development of porosity and enhancing the specific surface area of the hydrochar, thereby improving its suitability for the targeted applications (Zhao et al., 2020). Afterward, the obtained product was washed with deionized water and dried in a vacuum dryer at 80 °C for 12h to yield 58% of a black fluffy powder, calcined hydrochar. In order to compare the effectiveness of the hydrothermal carbonization process, the pristine material was also subjected to this multistep heat treatment, washing and drying at the same conditions to yield 22% of the so-called biochar. The mass yield of each product was determined using Equation 1:

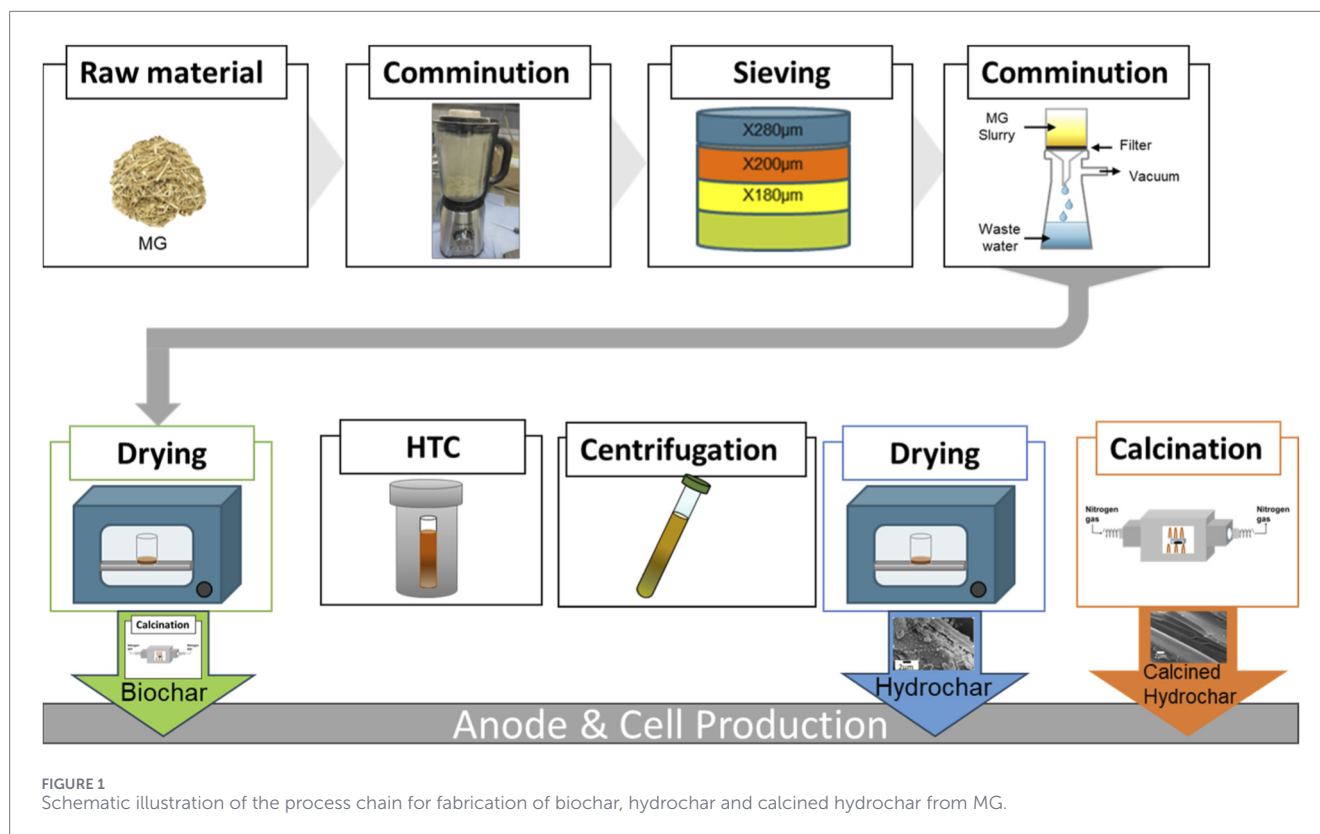
$$\text{Mass yield \%} = \frac{\text{Mass of dried product}}{\text{Mass of dried raw feedstock}} \times 100 \quad (1)$$

The pore volumes were calculated in agreement with the literature (Cavelan and Boussafir 2022) using Equation 2:

$$\text{Pore volume (cm}^3\text{/g)} = \frac{\text{amount of N}_2 \text{ adsorbed at } \frac{P}{P_0} = 0.99 \text{ (cm}^3\text{STP/g)}}{647(\text{N}_2 \text{ liquid volume ratio at 77K})} \quad (2)$$

2.3 Physicochemical characterization and sample preparation

The physicochemical characterization of the pristine biomass, hydrochar, calcined hydrochar and biochar was done using various methods. A Vario Micro Cube (Helium; WLD) from ELEMENTAR was employed for elemental analysis of carbon, hydrogen, and nitrogen. The oxygen content was calculated by subtracting the measured C, H, N, and ash contents from a total of 100%. For these measurements 15 mg sample mass of hydrochar and calcined hydrochar powders was used. The mass yields (%) of hydrochar was determined by measuring the weight of miscanthus powder before and the product after HTC. Similarly, the weights of the material before and after calcination at 800 °C for 2 h were recorded to calculate the calcined hydrochar yield. A comparable methodology was applied to biochar, where the weights of the powder before and after calcination at 800 °C for 2 h were taken to determine the biochar mass yields (Equation 1). The synthesized powders were further used for Fourier-transform infrared spectroscopy (FT-IR) using a VERTEX 70 device from Bruker. Thermogravimetric analysis was performed using a TGA/DSC1 STARE System from Mettler Toledo. A heating rate of 10 K min⁻¹ from 30 °C to 950 °C was employed under a nitrogen atmosphere. The morphology of hydrochar and calcined hydrochar was determined using scanning electron microscopy (SEM Helios G4 CX, Thermo Fisher Scientific). Raman spectroscopy using a WITec alpha 300 device was done in order to study the chemical properties of the synthesized hydrochar. XPS measurements were obtained on an AXIS Supra system (Kratos Analytical Ltd.) using a monochromatized Al α X-ray source. Survey scans were acquired using a pass energy of 160 eV. High-resolution spectra were obtained using a pass energy



of 20 eV. Data analysis was performed using the CasaXPS software. Materials were measured as powders, prepared on scotch tape (electrically isolated) and charge referenced to C 1s at 284.5 eV for graphitic/graphene (C=C) peak. For background correction a Shirley function was used, while the XPS signals were fitted using an LA Line Shape for graphene and GL for all other components (Biesinger 2022).

2.4 Cell fabrication and electrochemical characterization

The anode electrode was fabricated via a slurry casting technique employing hydrochar, calcined hydrochar, or calcined biochar as the active material. The active carbonaceous constituents were homogenized with conductive carbon black. The polymeric binder comprising carboxymethyl cellulose (CMC) and styrene-butadiene rubber (SBR) was prepared in a weight ratio of 5:15 wt.%. The overall composition of the slurry was maintained at a weight ratio of 70:20:10 (active material: carbon black: binder). Initially, the active material and carbon black were premixed using a tubular mixing apparatus for 1 hour to ensure uniform dispersion. Subsequently, this premix was integrated into a CMC aqueous dispersion, which had been pre-mixed also for an hour, followed by further stirring for an additional hour to achieve a homogeneous slurry. The slurry was then cast onto copper foil substrates using a Zehntner coater, followed by pre-drying at 60 °C for about 45 min prior to further drying at 80 °C for 12 h to facilitate solvent evaporation and binder consolidation. The resulting electrodes possessed an areal capacity of approximately 0.25 mA h cm⁻². Coin cells (CR2032-type) were assembled within an argon-filled

glovebox (H₂O < 1 ppm; GS GLOVEBOX Systemtechnik GmbH, Germany) to ensure an inert atmosphere. The cell architecture comprised a lithium metal counter electrode (Li foil, 500 µm thickness, Goodfellow), a polypropylene separator (Celgard 2500, 25 µm thickness, Celgard LLC), and an electrolyte consisting of 60 µL of 1 M LiPF₆ dissolved in a mixture of ethylene carbonate (EC) and dimethyl carbonate (DMC) in a 70:30 volume ratio (Sigma-Aldrich, 99.9%).

The assembly involved stacking the components as follows: a top cover, a 1 mm spacer, a 15 mm diameter lithium reference electrode, a 30-µL electrolyte layer, the separator, an additional 30-µL electrolyte, a 14 mm diameter anode, and a 0.8 mm spacer. The stack was secured with a wave spring, and the entire assembly was maintained at ambient temperature.

Electrochemical characterization was performed using a Maccor device, with galvanostatic charge-discharge cycling conducted within a potential window of 0.0–3.0 V at a current density of 186 mA g⁻¹. The rate capability was evaluated through a series of three-cycle tests at each C-rate (0.1 °C for formation, followed by 0.5 °C, 1.0 °C, 2 °C, and 5 °C), complemented by extended cycling at 0.5C to assess capacity retention and stability. All tests were performed at a controlled temperature of 25 °C following an initial formation period of 12 h. Electrochemical impedance spectroscopy (EIS) measurements were carried out using a Biologic SP-300 potentiostat, applying a perturbation amplitude of 10 mV over a frequency range from 100 kHz to 10 mHz. Cyclic voltammetry (CV) analyses were performed at a scan rate of 0.1 mV s⁻¹ within a potential window of 0.0–3.0 V to elucidate redox processes and interfacial kinetics.

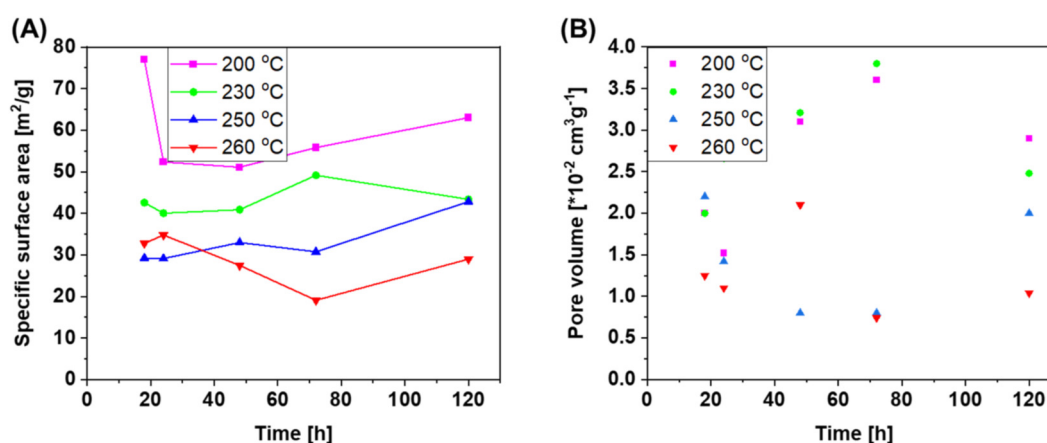


FIGURE 2

(A) Specific surface area of the obtained hydrochars determined via the Brunauer-Emmett-Teller (BET) method, (B) pore volume of the hydrochars for different residence times and temperatures.

3 Results and discussion

3.1 Optimization of hydrochar synthesis

Understanding and optimizing the structural and surface properties of hydrochar through controlled reaction parameters is crucial for tailoring its electrochemical performance, even when subsequent treatments like calcination are employed to enhance its suitability as an anode material in lithium-ion batteries.

3.1.1 Effect of reaction time

After hydrothermal carbonization at various residence times and target temperatures, the resulting hydrochars were comprehensively characterized, determining their specific surface area (SSA) and porosity. As visible in Figures 2A,B, the reaction time significantly influenced both the SSA and the total pore volume possibly due to the slow reactions occurring in the reactor, with the effect being contingent on the reaction temperature since it affects the properties of the subcritical water (Georgiou et al., 2021).

The obtained mass yield was determined for different residence times and different reaction temperatures as shown in Figure 3. Increasing the residence time from 18 to 120 h resulted in a decrease in the product mass from 61% to 48% at a temperature of 200 °C. Conversely, at elevated reaction temperatures, the product mass exhibited minimal reductions: from 46% to 45% at 230 °C, from 43% to 42% at 250 °C, and from 40% to 39% at 260 °C. These findings suggest that reaction temperature plays a predominantly influential role on the HTC reaction. However, as shown in Table 1, the carbon content shows to be much higher for all samples compared to the pristine material, with no clear trend being visible over the reaction time for all investigated reaction temperatures.

The significant decrease in product mass at 200 °C with extended residence time can be attributed to the rapid thermal degradation of hemicellulose and cellulose, leading to the formation of volatile compounds and gasification of both biomass and hydrochar (Wang et al., 2018; Zhang et al., 2021). In contrast,

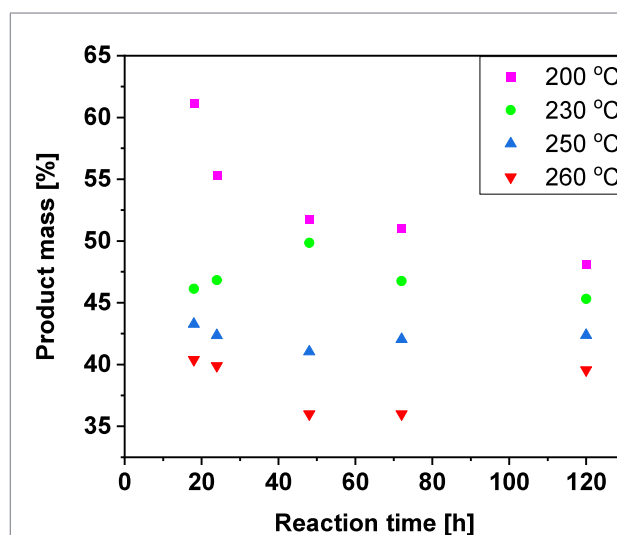


FIGURE 3

Hydrochar yields for different reaction times and temperatures.

at higher temperatures (230 °C, 250 °C, and 260 °C), while some decomposition of hydrochar still occurs, the decrease in yield is less pronounced (Zhang et al., 2021). At these elevated temperatures, the decomposition processes become more stabilized, requiring higher activation energies for further breakdown, which reduces the rate of gasification. Thus, while temperature plays a crucial role with respect to the product mass, the impact of residence time is significantly mitigated at temperatures above 200 °C.

The SEM images presented in Figures 4A–D (i–iii) reveal significant morphological modifications of the synthesized hydrochar as a function of reaction temperature and time. At 200 °C, increasing the reaction duration from 18 h to 72 h induces a transition from a smooth surface to a more wrinkled, rough texture, which is likely due to dehydration of the primary cell wall components of miscanthus. At 18 h and 200 °C, the hydrochar

TABLE 1 Data of the elemental analysis of hydrochar synthesized at different reaction temperatures (°C) and residence times (h) after on dry basis.

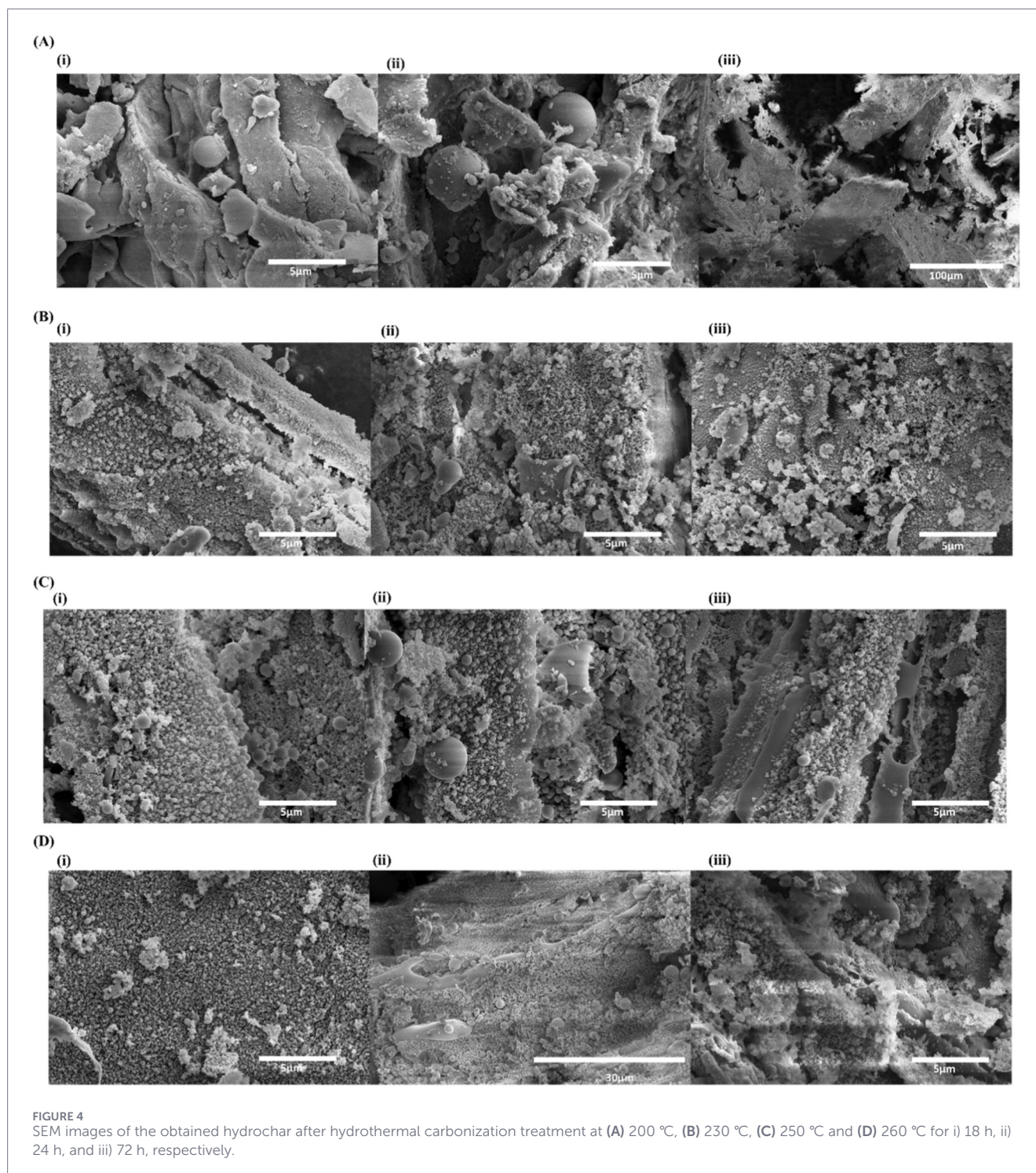
Reaction temp [°C]_ time [h]	Carbon (C)	Oxygen (O)	Hydrogen (H)	Nitrogen (N)
Pristine	47.06	46.81	5.94	0.19
200_18	77.35	9.27	13.30	0.08
200_24	58.90	35.53	5.37	0.20
200_48	63.77	31.03	5.04	0.16
200_72	66.59	28.41	4.80	0.20
200_120	67.27	27.87	4.61	0.25
230_18	69.51	25.35	4.92	0.22
230_24	71.01	23.92	4.85	0.22
230_48	74.59	20.45	4.65	0.31
230_72	68.90	26.21	4.64	0.25
230_120	69.30	25.81	4.62	0.28
250_18	71.60	23.15	4.98	0.27
250_24	72.19	22.61	4.94	0.26
250_48	73.26	21.38	4.97	0.39
250_72	73.09	21.62	4.97	0.32
250_120	73.17	21.65	4.89	0.29
260_18	69.34	25.73	4.60	0.33
260_24	74.68	20.08	4.90	0.34
260_48	69.27	25.91	4.50	0.32
260_72	70.66	24.36	4.50	0.49
260_120	74.13	20.70	4.83	0.36

predominantly displays large carbonaceous blocks with sparse nanospheres, indicative of initial carbonization. Prolonging the reaction time at this temperature results in the formation of additional nanospheres and an increase in SSA, reflecting enhanced porosity caused by exposure of pore structures, a trend that becomes more evident at 24 h. However, at 72 h, these features — wrinkles and nanospheres — disappear for higher reaction temperatures of 250 °C and 260 °C, likely due to agglomeration of the nanospheres, leading to surface deformation and a reduction in SSA and pore volume. This phenomenon is probably associated with lignin degradation, which begins near 255 °C, causing pore blockage and subsequent decrease in porosity, as supported by the observed decrease of SSA and pore volume in Figures 2A,B (Yu et al., 2019; Saha et al., 2019). These findings underscore the complex interplay between thermal treatment parameters and the morphological evolution of hydrochar, which critically influences its surface properties and potential applications.

Figure 5A shows that at reaction times of 24 and 48 h at a temperature of 200 °C, three characteristic but broad reflections at about 16°, 22°, 27° and 36° are observed. The first two reflections resemble those of the pristine material (fresh miscanthus following grinding, washing, and drying) and are attributed to the presence of cellulosic structures (I β -cellulose) (Randviir et al., 2019; Liu et al., 2017; Rios et al., 2020). The inorganic compounds

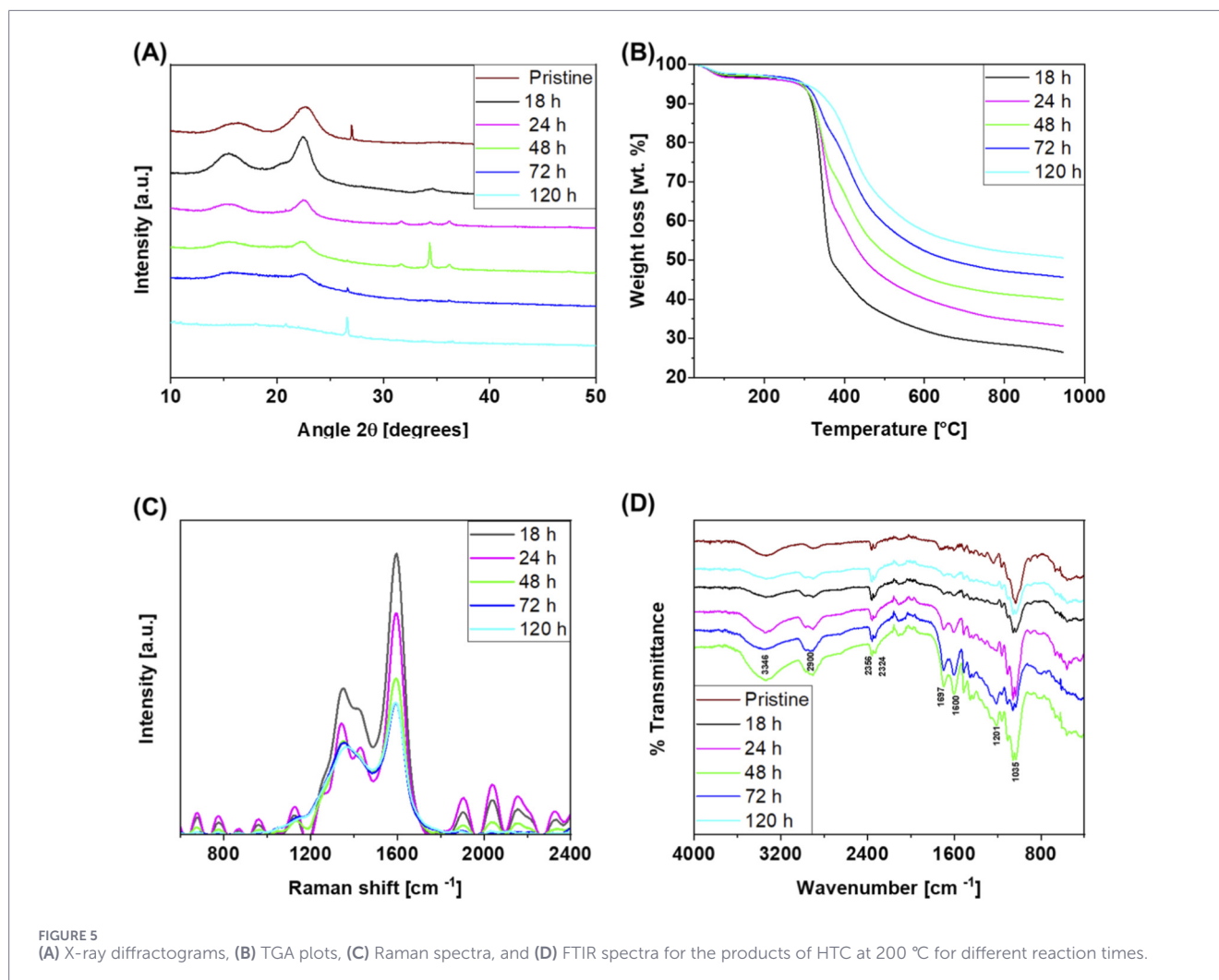
present in the MG samples, predominantly silica, are identified as hydrated silica, exhibiting reflections in the 20°–30° 2 θ range (Rios et al., 2020). This means that at this comparably mild temperature and short reaction time, the structure of the cellulose in miscanthus is preserved. However, as the reaction time increases to 72 and 120 h, cellulose degradation occurs as evidenced by the decrease and vanishing of the reflections at 16° and 22°. The sharp reflection observed at approximately 27° can be associated with the (002) plane of graphitic carbon domains. The gradual increase in its intensity with longer reaction times suggests an evolution toward a more ordered carbon structure, indicating a possible increase in the crystallinity of the hydrochar (Hamad et al., 2024).

Figure 5B presents the weight loss curves for the products of HTC at 200 °C after different reaction times of 18, 24, and 48 h. The decomposition process can be categorized into three stages: (1) moisture evaporation and low-boiling-point organic material (hemicellulose) release, (2) volatile matter decomposition, and (3) fixed carbon decomposition. The weight loss up to approximately 120 °C corresponds to moisture evaporation. A shoulder observed near 290 °C is linked to hemicellulose degradation, while a rapid weight loss at about 344 °C is attributed to cellulose degradation. Additionally, the weight loss at about 406 °C correspond to lignin degradation (Zhu et al., 2019). Hydrochar synthesized at shorter residence times (18 and 24 h) contained higher proportions of



hemicellulose and cellulose, which decompose into volatiles (CO , CO_2 , hydrocarbons, etc.) at lower temperatures. Consequently, their weight loss occurred earlier than those of hydrochar obtained after at longer residence times (72 and 120 h). This trend was also observed for the final weight loss minimum points above 400 °C. The thermograms indicate that the weight loss nicely shows the progress of the HTC reaction as evidenced by a reduction in weight loss from 74% for 18 h, to 77% for 24 h, and down to 50% for 120 h.

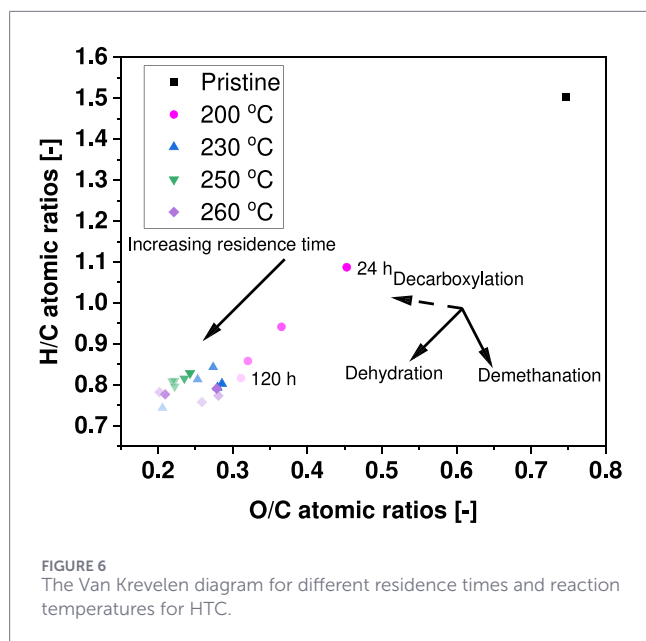
Figure 5C shows the Raman spectra of hydrochar synthesized after various HTC reaction times. In the course of the reaction, the degree of ordering in the hydrochar is changed. The characteristic Raman peaks at 1343 cm^{-1} and 1595 cm^{-1} correspond to the D and G bands, representing sp^3 hybridized carbon in a disordered state and sp^2 hybridized carbon in a graphitic structure, respectively (Jiang et al., 2016; Lim et al., 2020). As the reaction time increases from 18 to 120 h, there is an initial shift from a graphitic to a



disordered structure, evidenced by an increasing intensity ratio I_D/I_G of the two peaks from 0.521 to 0.66. These bands indicate the presence of sp^2 carbon atoms in benzene or condensed benzene rings, suggesting the presence of aromatic structures in the hydrochar (Sevilla and Fuertes 2009) as further supported by the FTIR results in Figure 5D. The FTIR spectra of the samples synthesized at 200 °C closely resemble those of the pristine material, indicating no significant chemical transformations during heat treatment at temperatures ≤ 200 °C. The presence of aromatic rings is indicated by the band at 1600 cm^{-1} , attributed to C=C vibrations, while the peak at 1697 cm^{-1} corresponds to C=O stretching vibrations, which may arise from carbonyl, quinone, ester, or carboxyl groups (Sevilla and Fuertes 2009). The peak at 1035 cm^{-1} corresponds to C–O stretching in aryl or alkyl ethers formed during the depolymerization and hydrolysis of cellulose and hemicellulose, with intensity increasing over time (Major et al., 2018). The peak at 1201 cm^{-1} is attributed to C–O stretching vibrations in hydroxyl, ester, or ether groups, as well as O–H bending vibrations, which significantly decrease only after prolonged reaction times 120 h (Sevilla and Fuertes 2009). This decrease typically indicates the complete removal of lignin (Barbash et al., 2019). The peaks at 2900 cm^{-1} correspond to C–H

functional groups in cellulose and increase with reaction time to 48 h followed by decrease up to 120 h. The broad peak at 3346 cm^{-1} is attributed to O–H stretching vibrations in hydroxyl or carboxyl groups. Its decrease relative to raw miscanthus indicates dehydration during hydrothermal carbonization (Sevilla and Fuertes 2009; Georgiou et al., 2021; Gamgoum et al., 2016). The diminishing intensity of these O–H peaks over time demonstrates the efficient removal of lignin and the occurrence of dehydration reactions in miscanthus (Barbash et al., 2019).

Figure 6 presents the Van Krevelen diagram displaying the H/C and O/C ratios from for various HTC temperatures and reaction times. The H/C and O/C ratios decreased from 1.087 to 0.453 at 200 °C and 24 h to 0.817 and 0.311 at 200 °C and 120 h, indicating that dehydration, demethanation, and decarboxylation occurred with increasing reaction time. A similar trend in H/C and O/C atomic ratios was observed across different HTC temperature conditions. Moreover, it can be inferred that the hydrothermal carbonization of miscanthus to hydrochar primarily follows a dehydration process, which aligns with the existing literature (Zhu et al., 2019; Qadi et al., 2019). The results demonstrate that at a constant reaction time, the carbon content increases with temperature, while the oxygen content decreases.



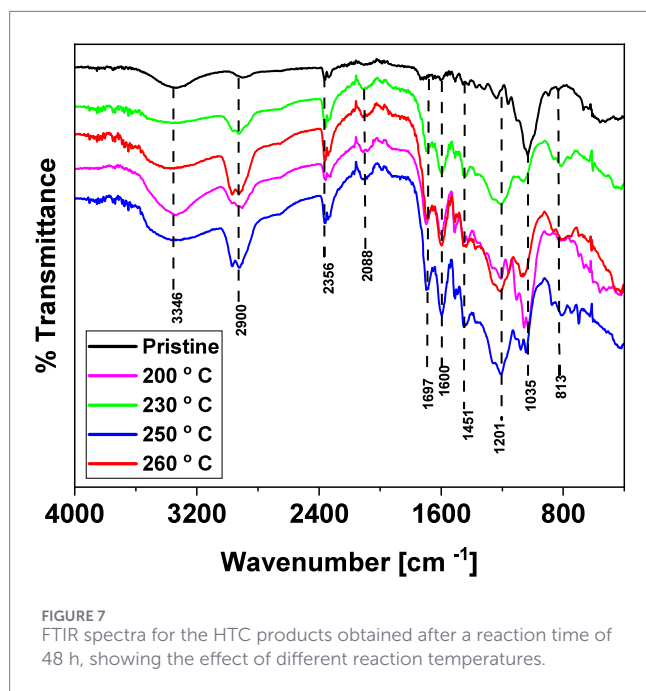
3.1.2 Effect of reaction temperature

The mass yield of the synthesized hydrochar, as illustrated in Figure 3, demonstrates a clear dependence on reaction temperature, with product mass e.g. decreasing from 62% at 200 °C to 41% at 260 °C for a reaction time of 18 h. This underscores the dominant effect of reaction temperature on the properties of miscanthus-derived hydrochar. This decrease can be attributed to the enhanced decomposition of hemicellulose and cellulose into smaller, volatile compounds (Wang et al., 2018; Zhang et al., 2021). The higher product mass of miscanthus hydrochar at 200 °C can be ascribed to the inherent stability of its structural composition during HTC, which promotes effective biomass conversion to hydrochar at this temperature. The HTC process significantly enhanced the yield of the carbon material after the calcination step, achieving a calcined hydrochar yield of approximately 58% relative to the mass of the pristine MG, markedly higher than the ~22% yield obtained from direct pyrolysis of biochar under equivalent heat treatment conditions. The measured C, H, O and N contents (Table 1) were in agreement with the reports of previous studies on hydrochar synthesized from MG at similar reaction temperatures, with the observed slight differences attributed to different reaction times and agroclimatic conditions (Georgiou et al., 2021; Zhang et al., 2021). A clear trend of increasing carbon content with elevated reaction temperature was observed, consistent with the progressive carbonization process (Funke and Ziegler 2010). The reduction in oxygen content with temperature is indicative of the dehydration and deoxygenation reactions characteristic of the HTC process (Qadi et al., 2019), and is corroborated by the decrease in the bands of oxygenated functional groups as evidenced by FTIR spectroscopy. In agreement with the established literature on HTC of biomass (Sevilla and Fuertes 2009b; Funke and Ziegler 2010), the nitrogen content of the hydrochar increased with increasing reaction temperature. Starting from an initial value of 0.19% in the pristine Miscanthus, the nitrogen content rose to 0.25% (200 °C), 0.28% (230 °C),

0.29% (250 °C), and 0.36% (260 °C). The incorporation and/or enrichment of nitrogen functional groups within the hydrochar structure is a well-documented phenomenon in HTC and is often considered beneficial for various energy storage mechanisms due to their potential to enhance electrochemical activity and ion diffusion (Qadi et al., 2019).

Collectively, the elemental analysis data unequivocally demonstrates that increasing the reaction temperature significantly drives the carbonization process, leading to higher carbon content, a reduction in oxygenated functionalities, and an increase in nitrogen-containing functional groups. These findings are in strong agreement with the observations from FTIR analysis. This compositional evolution with temperature highlights the tunability of the hydrochar properties through precise control of the HTC reaction conditions. After 24 h, the higher reaction temperatures resulted in a decreased specific surface area, as shown in Figure 2A.

The FTIR spectra of the HTC products after 48 h of reaction are shown in Figure 7. Reaction temperatures above 200 °C led to an increase in the relative intensities of the FTIR bands at 1697 cm^{-1} and 1600 cm^{-1} , indicating a predominance of carboxylic and aromatic moieties in the hydrochar, respectively. These unconjugated C=O groups of phenolic esters, characteristic of the lignin spectrum, increase with temperature due to the enhanced exposure of lignin following holocellulose degradation (Mihajlović et al., 2018; Georgiou et al., 2021). During hydrothermal carbonization, the content of carboxylic groups typically increases due to surface aromatization and polymerization of hydrochar. Literature indicates that the content of functional groups increases up to a certain reaction temperature—dependent on feedstock and parameters like time—after which it decreases due to thermal decomposition at elevated temperatures (Saha et al., 2019; Bansal and Goyal 2005; Sevilla and Fuertes 2009b). Additionally, the intensity of the band at 3346 cm^{-1} , associated with stretching vibrations of functional hydroxyl (O–H) groups from hydroxyl, methyl, and methylene moieties in cellulose, diminishes with increasing temperature as was observed for an increase in reaction time, as cellulose degradation to smaller compounds is initiated around 220 °C (Georgiou et al., 2021). At temperatures above 200 °C, the peak at 813 cm^{-1} likely arises from aromatic C–H bonds resulting from aromatization and polymerization (Sevilla and Fuertes 2009b). The peak at 2900 cm^{-1} is attributed to the asymmetric and symmetric stretching of methyl and methylene groups in microcrystalline cellulose. Above 200 °C, the intensities of FTIR bands characteristic of lignin — at 1600 cm^{-1} (aromatic C=C), 1451 cm^{-1} (C–H deformation), and 813 cm^{-1} (aromatic C–H) which are reported as signature of the aromatization of hydrochar — increase with rising HTC temperature, likely due to the degradation of hemicellulose and cellulose, resulting in a higher proportion of lignin (Mihajlović et al., 2018; Elmay et al., 2015; Gamgoum et al., 2016). The characteristic cellulose bands for C–O stretching at 1040 cm^{-1} as well as the asymmetric C–O–C stretching band at 1161 cm^{-1} , are present only at 200 °C, arising from hemicellulose degradation, and vanish at higher temperatures due to cellulose degradation. The 2088 cm^{-1} band corresponds to allene groups in the aromatic rings, and its increasing intensity with higher reaction temperatures indicates enhanced aromaticity in the hydrochar (Hessien 2023; Njoku et al., 2015).



The diffractograms in Figure 8A indicate that after HTC at temperatures exceeding 200 °C, the characteristic reflections at 15°, 22°, and 35° associated with cellulosic structures are absent, as cellulose degradation initiates at 220 °C (Sevilla and Fuertes 2009; Rios et al., 2020). This indicates that, at relatively mild HTC temperatures of 200 °C, the hydrochar still possesses a high cellulose content. However, as the reaction temperature increases, a transition toward predominantly amorphous structures occurs. The reflection at 26° suggests an ordered carbon structure with a low degree of graphitization, consistent with the Raman spectra in Figure 6B and the existing literature (Huang et al., 2019). Hydrochar formation encompasses thermal and chemical processes — including dehydration, decarboxylation, and polymerization — that induce transitions between amorphous and semi-crystalline structural states. Among the biomass components, cellulose is inherently crystalline, whereas hemicellulose and lignin predominantly exist in amorphous forms. Therefore, the overall crystallinity of hydrochars is primarily determined by the relative content of crystalline cellulose in relation to amorphous constituents such as hemicellulose, lignin, extractives, and amorphous cellulose.

As shown in Figure 8B, hydrochar produced at temperatures of 230, 250, and 260 °C exhibited two distinct thermal degradation steps: a slight mass loss step at approximately 50 °C, and strong mass loss over a broader temperature range centered around 420 °C. A notable increase in the degradation temperatures with elevated HTC reaction temperature was observed, suggesting enhanced thermal stability related to the reaction temperature and duration. The initial weight loss observed below 100 °C is attributable to moisture evaporation, while the subsequent loss starting at 260 °C is likely linked to the volatilization of surface-associated small organic compounds present in the hydrochar synthesized at 200 °C. With increasing reaction temperatures, the weight loss observed between 300 °C and 450 °C is indicative of the thermal degradation of low-molecular-weight organic volatiles, including hemicellulose

and cellulose, as well as the combustion of higher-molecular-weight components such as lignin and fixed carbon (Zhang et al., 2021). These findings suggest that thermal stability increases with higher reaction temperatures, where the carbonization efficiency of the miscanthus biomass is enhanced.

3.2 Characterization of calcined hydrochar and biochar

Based on the above results, the HTC conditions of 230 °C temperature and 48 h reaction time were chosen as the standard conditions for further investigation. Table 2 provides a comparison of the specific surface area and porosity of the hydrochar product under these conditions with the biochar and calcined hydrochar obtained after calcination at 800 °C of the MG precursor material and the hydrochar, respectively. The N₂-BET surface area of calcined hydrochar was the highest amounting to 450 m² g⁻¹ followed by that of biochar with 350 m² g⁻¹ and the hydrochar with 40 m² g⁻¹. This is in agreement with literature because hydrochars are usually amorphous materials with very low microporosity. With calcination, the biomass loses more volatile matter leading to an increase in pore volume and consequently in specific surface area, which is in agreement with the literature. However, although both the biochar and calcined hydrochar were subjected to the same multistep calcination treatment, the calcined hydrochar developed a better pore network and hence higher specific surface area because of the already established structure introduced by the hydrothermal carbonization step. From Table 3, it can be observed that the resulting calcined hydrochar had higher carbon and nitrogen contents that are known to lead to better electrochemical performance compared to biochar. Furthermore, looking at the shapes of the adsorption and desorption curves in Figure 9A even a clearer difference between the two synthesis routes becomes evident. After the HTC treatment, the hydrochar and calcined hydrochar had type IV isotherms with the hysteresis usually associated with micro-mesoporous carbon. This property is useful for lithium-ion transport to and from the anode via adsorption and intercalation combination. In contrast, the biochar isotherm curve is that of type I with its characteristic concave shape to the P/P₀ axis, usually associated with microporous materials having narrow micropores (of width < 1 nm) and whose nitrogen uptake is limited by the accessible micropore volume rather than internal surface area.

In addition, the thermal properties of the three materials are compared. From the weight loss and differential weight loss of the biochar and calcined hydrochar (Figure 9B), it is observed that the calcined hydrochar had a higher moisture content compared to the biochar which is indicated by the weight loss up to about 180 °C, due to re-adsorbed water when leaving the sample under ambient conditions after calcination, with the higher SSA of the calcined hydrochar also leading to a larger adsorbed amount. Consequently, it can also be observed that the calcined hydrochar overall had a higher weight loss compared to biochar.

XPS analysis reveals a higher fraction of oxygen- and nitrogen-containing functional groups in the calcined hydrochar (9.74%) compared to biochar (8.01%), confirming that hydrothermal pretreatment introduces additional polar Li⁺ adsorption sites and improves electrode–electrolyte wettability (Shan et al., 2020; Marrochi et al., 2024). These surface

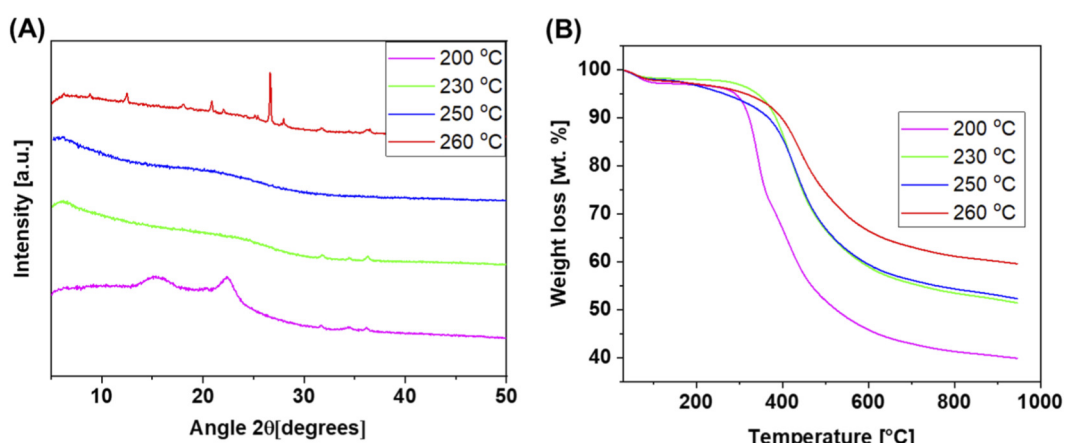


FIGURE 8 (A) X-ray diffractograms of the HTC products obtained after a reaction time of 24 h, and (B) thermograms of the hydrochar powders obtained after a reaction time of 48 h.

TABLE 2 Physical characteristics of the hydrochar, calcined hydrochar and biochar.

HTC [°C]	Calcination [°C]	S _{BET} [m ² g ⁻¹]	Pore volume [(×10 ⁻²) cm ³ g ⁻¹]
230	–	40.89	3.21
230	800	453.12	5.60
–	800	350.83	2.30

TABLE 3 Data of the elemental analysis of the final products compared to hydrochar on a dry basis.

Reaction temp [°C] _ time [h]	Carbon (C)	Oxygen (O)	Hydrogen (H)	Nitrogen (N)
Pristine	47.06	46.81	5.94	0.19
Hydrochar 230_48	74.59	20.45	4.65	0.31
Calcined hydrochar 800_2	91.28	6.90	1.58	0.24
Biochar 800_2	87.61	11.37	0.85	0.17

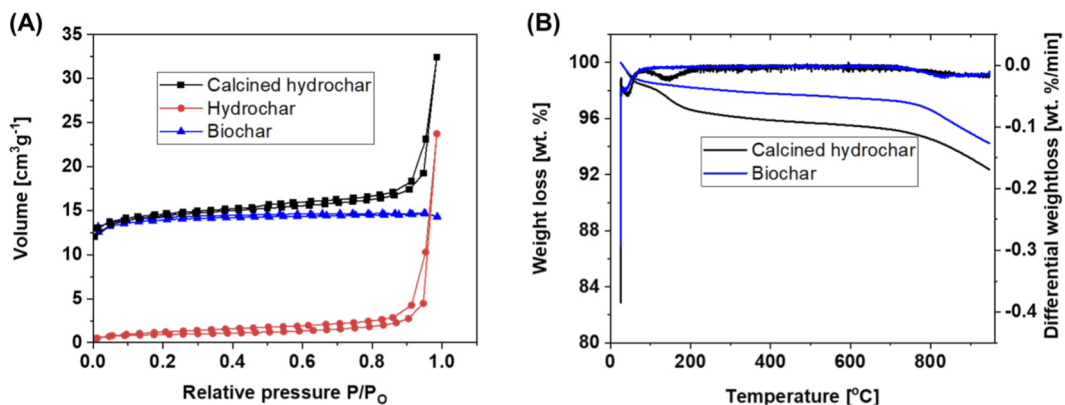


FIGURE 9 (A) Nitrogen adsorption and desorption isotherms and (B) TGA and DTG plots for the calcined hydrochar, hydrochar and biochar samples prepared at the chosen optimum conditions.

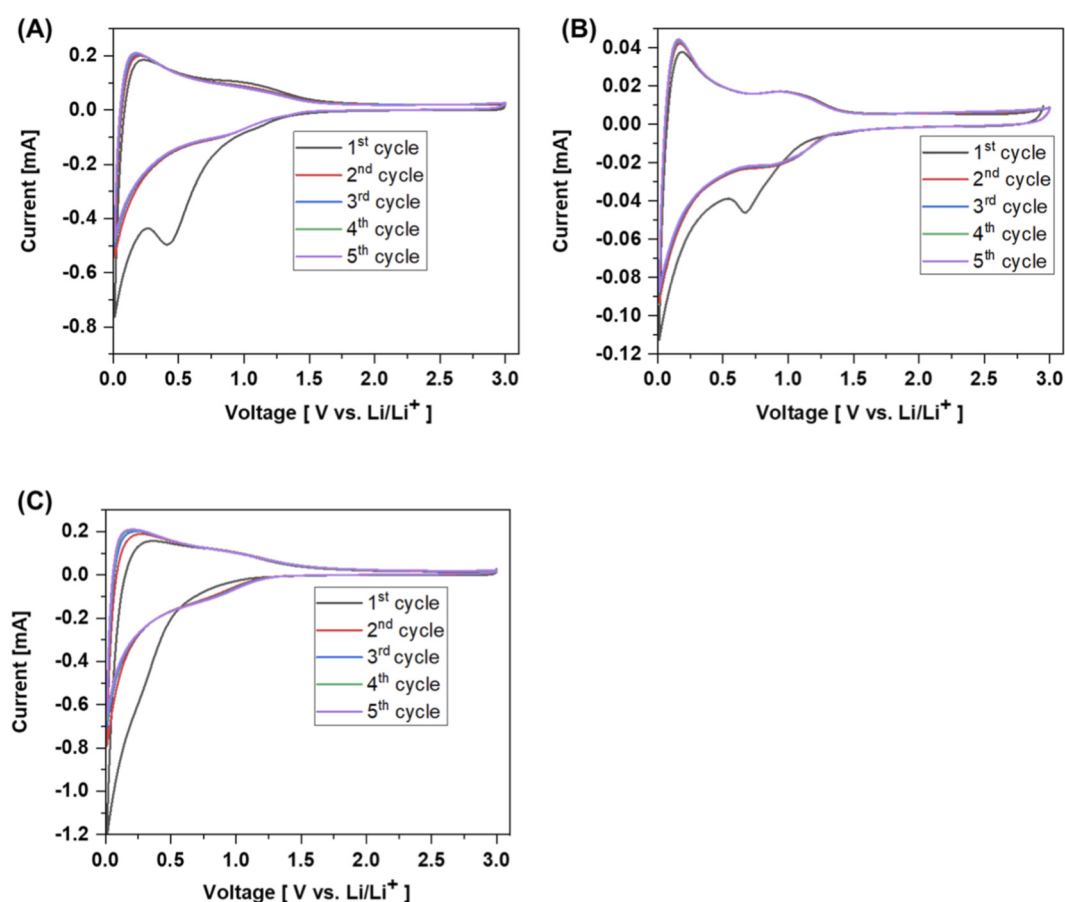


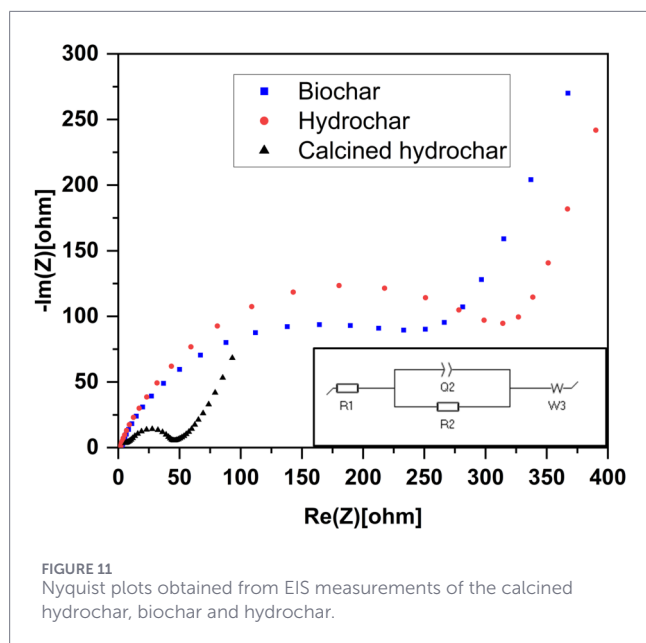
FIGURE 10 Cyclic voltammety measurements at a scanning rate of 0.1 mV s^{-1} for (A) the calcined hydrochar, (B) the hydrochar and (C) the biochar.

functionalities and the associated hierarchical porosity accelerate ion/electron transport and enable markedly enhanced electrochemical kinetics relative to biochar.

3.3 Electrochemical characterization

To comprehensively assess the lithium-ion storage capabilities of the synthesized hydrochar, calcined hydrochar, and biochar, a series of electrochemical measurements were conducted. Figure 10 shows the cyclic voltammety (CV) curves of hydrochar, calcined hydrochar and biochar in five cycles tested at a scanning rate of 0.1 mV s^{-1} within a voltage range of 0.0–3.0 V. A typical cyclic voltammety curve of hard carbon materials was observed, whereby the first cycle differed considerably from the subsequent cycles (Luna-Lama et al., 2021; Luo et al., 2019). In the initial reduction cycle, cathodic peaks indicative of reversible Li-ion insertion was observed at 0.1 V for hydrochar, 0.01 V for calcined hydrochar, and 0.02 V for biochar. Additionally, moderate cathodic peaks were present at approximately 0.67 V and 0.42 V in the hydrochar and calcined hydrochar profiles, respectively, while being absent in the biochar data. The observed peaks can be attributed to electrolyte decomposition on the surface induced by the SEI formation and also to the irreversible insertion of lithium ions into special positions

in the carbon structure (Luna-Lama et al., 2021; Luo et al., 2019). Furthermore, the fact that these peaks were moderate and consistent with the charge-discharge curves (no clear plateaus) indicates that the uptake of Li ions in the anode was a combined effect of capacitive and intercalation behavior (Li et al., 2022). For all the tested carbons, the peak disappeared in the second and subsequent cycles which means that it is associated with irreversible reactions. The fact that the charging curves overlapped with the discharge curves is an indicator of the stability of the structure of the carbons (Luna-Lama et al., 2021; Luo et al., 2019) and good reversibility. In the region between 0.0 and 0.3 V a sharp reduction peak occurs which can be associated with the intercalation process of Li ions into the hydrothermally synthesized carbons (Luna-Lama et al., 2021; Luo et al., 2019). For all carbons, as seen in Figures 10A–C, there was an anodic peak at about 0.1 V with pronounced sharpness for the HTC-synthesized carbon, which is attributed to the deintercalation process of lithium ions from the stacked layers of the carbonaceous porous structure (Luna-Lama et al., 2021). This means that the deintercalation process was improved for the hydrochar as compared to the biochar. From the shape of the CV diagrams, it is clear that calcined hydrochar and hydrochar have a reversible redox mechanism while the biochar sample only shows an irreversible redox mechanism. The appearance of a “hump” between



0.5 and 1.2 V is also more pronounced for the HTC-synthesized carbons, and is attributed to the adsorption-desorption processes of the lithium ions from the carbon structure. Since the prevalence of both intercalation/deintercalation and adsorption/desorption of the lithium ions depends on the degree of graphitization, the porous structure and functional group and defects, it can be argued that HTC, which introduces a higher content of nitrogen and lower content of oxygenated functional groups, as well as porous structure with moderate specific surface areas, was key to the improved ion reversibility and diffusion. Furthermore, the CV area of calcined hydrochar was the highest followed by that of biochar and then hydrochar due to the more developed porous structure which provides a higher specific capacity. This further proves the importance of a calcination step after hydrothermal carbonization to improve the specific surface area and hence develop a more defined porous structure (Luna-Lama et al., 2021).

Figure 11 presents the Nyquist plots of the EIS data measured for anodes based on the hydrochar, calcined hydrochar and biochar. In all plots, the typical behavior of a single depressed semicircle from high to medium frequency and an inclined tail in the low-frequency region is visible. The first semicircle is correlated to combined effects of the contact between the interfaces, the electrode resistance and the resistance due to the SEI, given by R_e , in addition to the charge transfer resistance at the electrode/electrolyte interface, given by R_{ct} , while the tail (Warburg impedance), given by Z_w , is attributed to the diffusion of lithium ions into the carbon electrode. The calcined hydrochar had the smallest diameter of the semicircles with the lowest R_{ct} value of 27.7 Ω , while the hydrochar had an R_{ct} of 120.0 Ω and the biochar of 92.0 Ω . The low R_{ct} of the calcined hydrochar implies that this sample possessed the highest electrical conductivity and enables the most rapid charge transfer reaction for lithium-ion insertion and extraction of the three samples (Chen et al., 2014).

Figure 12 displays the galvanostatic charge-discharge profiles at 0.1C and 0.5C, which are characteristic of amorphous carbons, exhibiting a continuous voltage change without distinct plateaus

(Li et al., 2022). In the initial cycle, the discharge capacities recorded for hydrochar, biochar, and calcined hydrochar were 36, 448, and 833 mA h g^{-1} , respectively, revealing pronounced disparities between the three samples. While the initial coulombic efficiencies amounted to 58, 54% and 51%, after the first cycle, the CE for the hydrochar, biochar and calcined hydrochar increased to 89, 93% and 90%, respectively. The markedly elevated capacity of the calcined hydrochar is primarily attributed to its higher specific surface area and porosity, which facilitate enhanced electrolyte contact and Li-ion accommodation. Conversely, the hydrochar exhibits very low reversible capacity, which can be attributed to its residual volatile matter, ash content and limited porosity and surface area (Yu et al., 2021). Notably, aside from the hydrochar, which demonstrated minimal capacity degradation from the initial to the second cycle, the samples experienced significant capacity loss. This phenomenon is predominantly ascribed to the formation and stabilization of the SEI layer, which occurs due to the catalytic reduction of electrolyte constituents at the electrode-electrolyte interface. The increased specific surface area of the active material, coupled with the entrapment of lithium ions that intercalate into deep sites within the carbon matrix, results in a higher irreversible capacity loss. These lithium ions, which become deeply embedded within the carbon structure, are not fully recoverable during subsequent charging cycles, thus exacerbating capacity fade (Yu et al., 2021). Despite this high-capacity loss, the cells based on the biochar and the calcined hydrochar still exhibited substantially higher capacity than the hydrochar-based cell. There was no significant change to the charge/discharge curves after the second cycle, implying good reversibility and stability of all the carbon electrode materials (Wang et al., 2016; Wan and Xiaofang Hu 2019). As the SEI suppresses electrolyte decomposition, the reversible capacity stabilizes after the first cycle, to about 360 mA h g^{-1} for the biochar and about 800 mA h g^{-1} for the calcined hydrochar, revealing good reversibility for the anode materials. For hydrothermally synthesized carbon materials, analogous phenomena have been reported in the limited literature addressing biobased carbons (Campbell et al., 2015; Luna-Lama et al., 2021).

The long-term cycling behavior of the different half cells is shown in Figure 13A. Notably, an increase in the discharge capacity was observed with cycling, reaching values of approximately 120 mA h g^{-1} for the hydrochar and exceeding 700 mA h g^{-1} for the calcined hydrochar after 350 cycles. For continued cycling to 500 cycles, the discharge capacity for the hydrochar even increases further to more than 200 mA h g^{-1} , whilst for the calcined hydrochar some decrease to about 600 mA h g^{-1} is observed. This capacity augmentation has been attributed to an unconventional mechanism whereby the initial SEI film undergoes rupture, facilitating the formation of a new, thinner SEI layer, thereby enhancing the reversible capacity (Luna-Lama et al., 2021). Additionally, the intrinsic nanoarchitecture and the increased content of nitrogen functional groups introduced during HTC contribute to defect formation within the carbon matrix, generating numerous active sites conducive to Li-ion storage (Román et al., 2013). This phenomenon is further rationalized by the progressive exposure of previously inaccessible mesopores and micropores, which become accessible following SEI rupture induced by repeated cycling (Campbell et al., 2015). Consequently, increased electrolyte contact enhances the electrochemical activity, leading

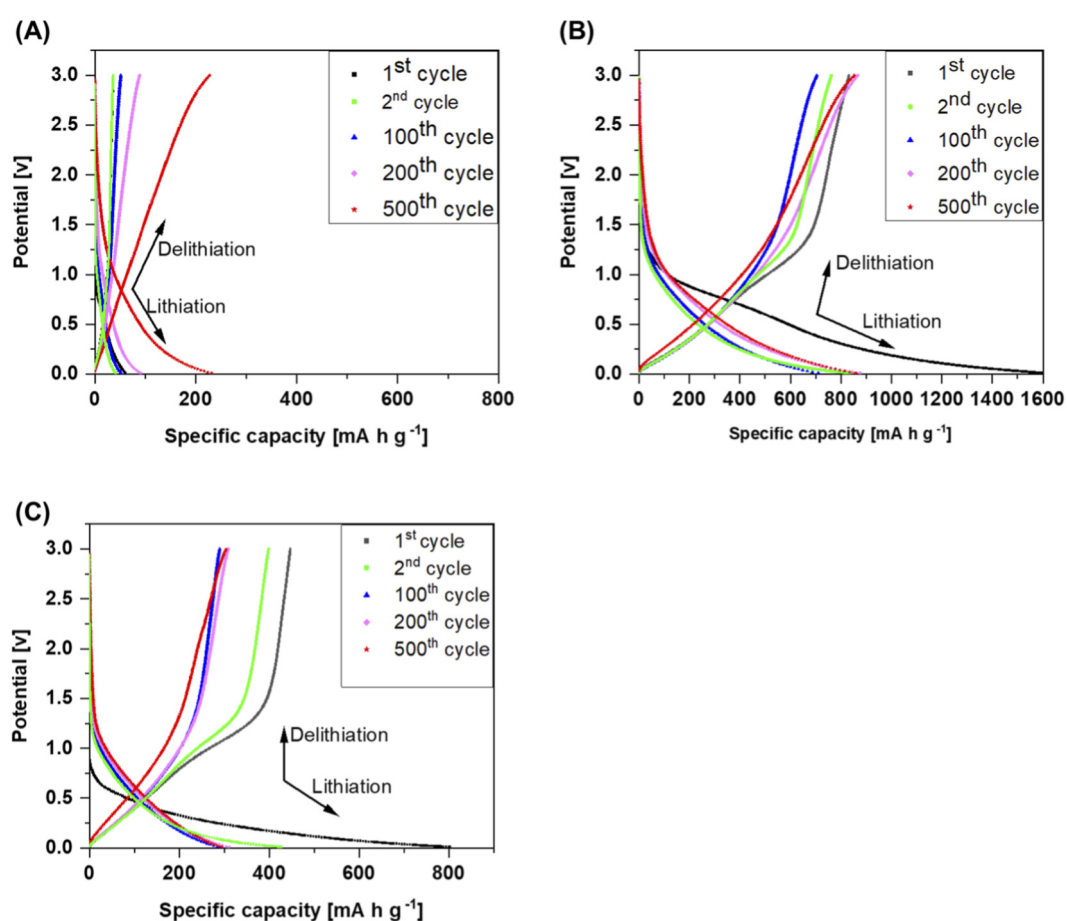


FIGURE 12 Galvanostatic charge-discharge curves for a half-cell based on (A) the hydrochar, (B) the calcined hydrochar and (C) the biochar at a C-rate of 0.1 (1st and 2nd cycles) and 0.5C (100th, 200th and 500th cycles).

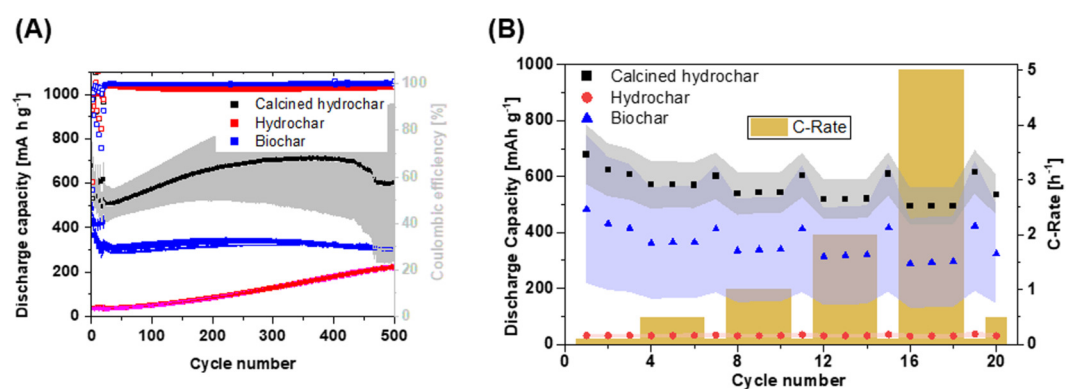


FIGURE 13 (A) Long-term cycling data of half-cells containing anodes based on the hydrochar, biochar, and the calcined hydrochar at a C-rate of 0.5, and (B) rate capability test for half-cells with anodes based on the hydrochar, biochar and the calcined hydrochar at different C-Rates.

to higher specific capacities through ongoing oxidation/reduction processes at the anode interface. Interestingly, non-activated carbons have demonstrated superior specific discharge capacities over

cycling compared to activated carbons, particularly at elevated C-rates (Campbell et al., 2015). Also in this study, the observed high capacities of calcined hydrochar surpass the values reported

TABLE 4 A comparison of specific capacities of activated carbons as anodes from different synthesis routes and for different biomass.

Biomass precursor	Chemical pretreatment	Method/Temp [°C]	Activation media/Temp [°C]	S _{BET} [m ² g ⁻¹]	Plateau capacity [mAh g ⁻¹]	Current density [mA g ⁻¹]	Application	Reference
Lotus stem		Carbonization/1400			250	100	NalBs	Zhang et al. (2018)
Reed flowers		HTC/220	KOH/800	1714.83	581.2	100	LIBs	Zhao et al. (2020)
Alkali lignin			Pyrolysis/750	419.24	225	60	LIBs	Zhao et al. (2016)
Bacteria cellulose		HTC/200	Pyrolysis/800		935	0.1	LIBs	Zhang et al. (2016)
Peanut dregs		HTC/180	Pyrolysis/900 KCl, FeCl ₃ , C ₂ H ₄ N ₄	334	6.27	1.5	LIBs	Yuan et al. (2020)
Sisal fibre			Pyrolysis	616.4	646	1	LIBs	Yu et al. (2015)
Corn straw	H ₂ SO ₄	HTC/200	Pyrolysis/600	402	577	0.2C	LIBs	Yu et al. (2019)
Rice husk		Carbonization/500	Pyrolysis/750/NaOH	2176	448	0.2C	LIBs	Yu et al. (2018)
<i>Miscanthus × giganteus</i>		Pyrolysis/700	Pyrolysis/900 KOH	3024		0.05V s ⁻¹	EDLC	You et al. (2018)
Cotton balls	Mg(NO ₃) ₂ Thiourea	Pyrolysis/800			1101.1	0.2 A/g	LIBs	Xiong et al. (2018)
Reed flowers		HTC/220	Pyrolysis/80000 KOH	1712.6	908	0.1C	LiS	Wang et al. (2020)
Hemp haulm		Pyrolysis/600			256	0.1C	NalBs	Wang et al. (2020)
Bamboo biochar		Pyrolysis/800/1000		310	250	0.2C	LIBs	Barbosa Nogueira et al. (2025)
Rice husk	HCOOH	HTC/230	Pyrolysis/900	243	372	75mA g ⁻¹	LIBs	Wang et al. (2013)
Rice husk		Hydrolysis/H ₂ SO ₄ /95	Pyrolysis/H ₃ PO ₄ /500 Pyrolysis/800 KOH	2700 2488				Wang et al. (2010)
Peanut skin	KOH	HTC/H ₂ SO ₄ /180	Pyrolysis/800/KOH	2500	431	0.1A/g	NalBs	Wang et al. (2016)
Hazelnut shells HN-MA	Magnesium acetate tetrahydrate (MgAc)		Pyrolysis/800	1580	174			
<i>Miscanthus × giganteus</i>		HTC/230	Pyrolysis/600/MgO	150	307	1C	LIBs	Unur et al. (2013)
			Pyrolysis/800	453*	700*	0.5C	LIBs	This work

*These values were obtained in this research work.

for activated carbon materials in the literature — for instance, those reported for chemically activated corn straw-derived carbon (577 mA h g⁻¹ at 0.2 °C) (Yu et al., 2019), and banana peel-based carbon chemically activated with various agents such as phosphoric acid (272 mA h g⁻¹ at 0.2 °C) (Luna-Lama et al., 2021). This underscores the efficacy of our green hydrothermal carbonization and calcination strategy in producing high-performance carbon materials for lithium-ion battery anodes, without resorting to harsh and environmentally detrimental chemical activation processes. It is also pertinent to note that samples characterized by high carbon content and low oxygen functionalization tend to exhibit higher degrees of structural order and aromaticity, which minimizes the extent of first-cycle irreversible capacity loss by controlling SEI formation.

The rate capability of anode materials is a critical parameter determining their practical applicability in lithium-ion batteries. As depicted in Figure 13B, the results reveal that increasing the C-rate from 0.1 °C to 0.5 °C led to a decrease in discharge capacity from approximately 678.0 mA h g⁻¹–569.8 mA h g⁻¹ for calcined hydrochar, and from 484.1 mA h g⁻¹–362.4 mA h g⁻¹ for biochar. Subsequent escalation to 1 °C resulted in capacities of 539.3 mA h g⁻¹ and 335.0 mA h g⁻¹ for calcined hydrochar and biochar, respectively, while at 5 °C, capacities further declined to 494.2 mA h g⁻¹ and 289.8 mA h g⁻¹. Notably, after 15 cycles at high C-rates, when the current density was reverted to 0.5 °C, the cells retained their previous capacities, with calcined hydrochar and biochar exhibiting a capacity resurgence to only slightly lower values than previously achieved, indicating potential activation phenomena. A similar trend was observed for the hydrochar-based cell, albeit with capacities below the resolution scale of the figure.

These findings demonstrate that the calcined hydrochar exhibits superior capacity and rate performance compared to the biochar and hydrochar, and even outperforms many chemically activated carbons documented in the literature (see Table 4 for an extensive comparison). The enhanced electrochemical kinetics can be attributed to the high degree of structural order, coupled with a well-developed network of micropores and mesopores, which collectively facilitate rapid Li-ion transport by providing unobstructed pathways.

3 Conclusion

In this study, we reported the synthesis of novel biobased carbon materials derived from *Miscanthus × giganteus* via an environmentally sustainable, green hydrothermal carbonization process. This facile, eco-friendly, and catalyst-free approach obviates the need for complex chemical activation procedures and hazardous chemical wastes. The hydrothermal carbonization was conducted at 230 °C, followed by calcination at 800 °C to optimize the physicochemical properties of the resulting hydrochar, with reaction temperature identified as a critical parameter influencing structure and porosity.

The hydrochar produced at 230 °C with a reaction time of 48 h exhibited a high yield of approximately 48% and favorable specific surface area and porosity characteristics. Characterization revealed a higher content of nitrogen functional groups and reduced oxygen

functionalities, correlated with improved electrical conductivity and electrochemical activity. The preservation of hierarchical architecture and interlayer spacing likely facilitates lithium-ion intercalation, contributing to enhanced capacity retention and cycling stability.

Electrochemical evaluation of the calcined hydrochar demonstrated exceptional performance as an anode material for lithium-ion batteries, delivering a reversible capacity exceeding 700 mA h g⁻¹ at 0.5 C after 400 cycles, with Coulombic efficiency close to 100%. This performance is attributed to the favorable porous nanostructure, inherent self-activating elements such as silicon, nitrogen-containing surface functionalities, and enhanced electrical conductivity. Moderate specific surface area further limits parasitic side reactions, enabling superior cycling stability compared to conventional activated carbons.

Overall, this work demonstrates a cost-effective, scalable, and environmentally benign strategy for producing high-performance biomass-derived carbons from *Miscanthus × giganteus*, offering a sustainable alternative to conventional graphite for next-generation energy storage applications.

Data availability statement

The raw data supporting the conclusions of this article will be made available by the authors, without undue reservation.

Author contributions

FK: Conceptualization, Investigation, Writing – original draft. RJ: Validation, Data curation, Writing – review and editing. PH: Writing – review and editing, Methodology. AJ-F: Writing – review and editing, Conceptualization, Supervision. GG: Resources, Supervision, Conceptualization, Funding acquisition, Writing – review and editing.

Funding

The author(s) declared that financial support was received for this work and/or its publication. This study was partially supported by the German Academic Exchange Service (DAAD) for the scholarship of Mr. Fabisch Kilonzi (Personal Ref. no.: 91694156). The author would also like to thank the “Deutsche Forschungsgemeinschaft” (DFG) (INST 188/444-1 FUGB).

Acknowledgements

The authors would like to acknowledge the German Academic Exchange Service (DAAD) for the scholarship of Fabisch Kilonzi (Personal Ref. no.: 91694156). We would also like to acknowledge Daniela Scholz for performing TGA, FTIR and XPS measurements, Wibke Dempwolf for XPS measurements and Bogdan Semenko for the SEM images.

Conflict of interest

The author(s) declared that this work was conducted in the absence of any commercial or financial relationships that could be construed as a potential conflict of interest.

Generative AI statement

The author(s) declared that generative AI was not used in the creation of this manuscript.

Any alternative text (alt text) provided alongside figures in this article has been generated by Frontiers with the support of artificial intelligence and reasonable efforts have been made to ensure accuracy, including review by the authors wherever possible. If you identify any issues, please contact us.

References

- Agubra, V. A., and Fergus, J. W. (2014). The formation and stability of the solid electrolyte interface on the graphite anode. *J. Power Sources* 268 (8), 153–162. doi:10.1016/j.jpowsour.2014.06.024
- Al Rai, A., and Yanilmaz, M. (2021). High-performance nanostructured bio-based carbon electrodes for energy storage applications. *Cellulose* 28 (9), 5169–5218. doi:10.1007/s10570-021-03881-z
- Bansal, R. C., and Goyal, M. (2005). *Activated carbon adsorption*. Boca Raton: Taylor & Francis.
- Barbash, V. A., Yashchenko, O. V., and Vasylyeva, O. A. (2019). Preparation and properties of nanocellulose from *Miscanthus × giganteus*. *J. Nanomater.* 2019, 3241968. doi:10.1155/2019/3241968
- Barbosa, N., Savio, L., Divitini, G., Pasquale, L., Chauque, S., Sperati, V., et al. (2025). Untreated bamboo biochar as anode material for sustainable lithium ion batteries. *Biomass Bioenergy* 193, 107511. doi:10.1016/j.biombioe.2024.107511
- Biesinger, M. C. (2022). Accessing the robustness of adventitious carbon for charge referencing (correction) purposes in XPS analysis: insights from a multi-user facility data review. *Appl. Surf. Sci.* 597, 153681. doi:10.1016/j.apsusc.2022.153681
- Campbell, B., Ionescu, R., Favors, Z., Ozkan, C. S., and Ozkan, M. (2015). Bio-derived, binderless, hierarchically porous carbon anodes for Li-Ion batteries. *Sci. Reports* 5, 14575. doi:10.1038/srep14575
- Cavelan, A., and Boussafir, M. (2022). Does grain size influence hydrocarbons generation and mesoporosity during artificial thermal maturation of an organic-rich mudstone? *J. Petroleum Sci. Eng.* 208, 109643. doi:10.1016/j.petrol.2021.109643
- Chen, L., Zhang, Y., Lin, C., Yang, W., Meng, Y., Guo, Y., et al. (2014). Hierarchically porous nitrogen-rich carbon derived from wheat straw as an ultra-high-rate anode for lithium ion batteries. *J. Mater. Chem. A* 2 (25), 9684–9690. doi:10.1039/c4ta00501e
- Chen, F., Yang, J., Bai, T., Long, B., and Zhou, X. (2016). Facile synthesis of few-layer graphene from biomass waste and its application in lithium ion batteries. *J. Electroanal. Chem.* 768, 18–26. doi:10.1016/j.jelechem.2016.02.035
- Deng, J., Li, M., and Wang, Y. (2016). Biomass-derived carbon: synthesis and applications in energy storage and conversion. *Green Chem.* 18 (18), 4824–4854. doi:10.1039/c6gc01172a
- Ding, L., Zou, B., Li, Y., Liu, H., Wang, Z., Zhao, C., et al. (2013). The production of hydrochar-based hierarchical porous carbons for use as electrochemical supercapacitor electrode materials. *Colloids Surfaces A Physicochem. Eng. Aspects* 423, 104–111. doi:10.1016/j.colsurfa.2013.02.003
- Dou, Y., Liu, X., Yu, K., Wang, X., Liu, W., Liang, J., et al. (2019). Biomass porous carbon derived from jute fiber as anode materials for lithium-ion batteries. *Diam. Relat. Mater.* 98, 107514. doi:10.1016/j.diamond.2019.107514
- Elmay, Y., Le Brech, Y., Delmotte, L., Dufour, A., Brosse, N., and Gadiou, R. (2015). Characterization of miscanthus pyrolysis by DRIFTS, UV Raman spectroscopy and mass spectrometry. *J. Anal. Appl. Pyrolysis* 113, 402–411. doi:10.1016/j.jaap.2015.03.004
- Feng, Y., Tao, L., Zheng, Z., Huang, H., and Lin, F. (2020). Upgrading agricultural biomass for sustainable energy storage: Bioprocessing, electrochemistry, mechanism. *Energy Storage Mater.* 31, 274–309. doi:10.1016/j.ensm.2020.06.017
- Funke, A., and Ziegler, F. (2010). Hydrothermal carbonization of biomass: a summary and discussion of chemical mechanisms for process engineering. *Biofuels, Bioprod. Bioref.* 4 (2), 160–177. doi:10.1002/bbb.198
- Gamgoum, R., Dutta, A., Santos, R., and Yi, C. (2016). Hydrothermal conversion of neutral sulfite semi-chemical red liquor into hydrochar. *Energies* 9 (6), 435. doi:10.3390/en9060435
- Gao, Y., Zhang, W., Yue, Q., Gao, B., Sun, Y., Kong, J., et al. (2014). Simple synthesis of hierarchical porous carbon from *Enteromorpha Prolifera* by a self-template method for supercapacitor electrodes. *J. Power Sources* 270, 403–410. doi:10.1016/j.jpowsour.2014.07.115
- Georgiou, E., Mihajlović, M., Petrović, J., Anastopoulos, I., Dosche, C., Pashalidis, I., et al. (2021). Single-stage production of miscanthus hydrochar at low severity conditions and application as adsorbent of copper and ammonium ions. *Bioresour. Technology* 337, 125458. doi:10.1016/j.biortech.2021.125458
- Gu, X., Lai, C., Liu, F., Yang, W., Hou, Y., and Zhang, S. (2015). A conductive interwoven bamboo carbon fiber membrane for Li-S batteries. *J. Mater. Chem. A* 3 (18), 9502–9509. doi:10.1039/C5TA00681C
- Hamad, N., Galhoum, A. A., Saad, A., and Wageh, S. (2024). Efficient adsorption of cationic and anionic dyes using hydrochar nanoparticles prepared from Orange peel. *J. Mol. Liq.* 409, 125349. doi:10.1016/j.molliq.2024.125349
- Hessien, M. (2023). Methylene blue dye adsorption on iron oxide-hydrochar composite synthesized via a facile microwave-assisted hydrothermal carbonization of pomegranate peels' waste. *Molecules* 28 (11), 4526. doi:10.3390/molecules28114526
- Huang, G.-ge, Liu, Y.-fei, Wu, X.-xing, and Cai, J.-jun (2019). Activated carbons prepared by the KOH activation of a hydrochar from garlic peel and their CO₂ adsorption performance. *New Carbon Mater.* 34 (3), 247–257. doi:10.1016/S1872-5805(19)60014-4
- Jiang, Q., Zhang, Z., Yin, S., Guo, Z., Wang, S., and Feng, C. (2016). Biomass carbon micro/nano-structures derived from ramie fibers and corncobs as anode materials for lithium-ion and sodium-ion batteries. *Appl. Surf. Sci.* 379 (7), 73–82. doi:10.1016/j.apsusc.2016.03.204
- Li, Y., Meas, A., Shan, S., Yang, R., and Gai, X. (2016). Production and optimization of bamboo hydrochars for adsorption of Congo red and 2-Naphthol. *Bioresour. Technology* 207, 379–386. doi:10.1016/j.biortech.2016.02.012
- Li, S., Luo, W., He, Q., Lu, J., Du, J., Tao, Y., et al. (2022). A lignin-based carbon anode with long-cycle stability for Li-ion batteries. *Int. J. Mol. Sci.* 24 (1), 284. doi:10.3390/ijms24010284
- Li, H., Song, L., Huo, D., Yang, Y., Zhang, N., and Liang, J. (2023). Cattail-grass-derived porous carbon as high-capacity anode material for Li-Ion batteries. *Molecules* 28 (11), 4427. doi:10.3390/molecules28114427
- Libich, J., Máca, J., Vondrák, J., Čech, O., and Sedlářková, M. (2017). Irreversible capacity and rate-capability properties of lithium-ion negative electrode based on natural graphite. *J. Energy Storage* 14 (5): 383–390. doi:10.1016/j.est.2017.03.017
- Lim, G. H., Chae, J., Cha, Y. L., Kang, Y. C., and Roh, K. C. (2020). Giant-miscanthus-derived activated carbon and its application to Lithium sulfur batteries. *Carbon Lett.* 30 (5), 477–484. doi:10.1007/s42823-019-00117-w
- Liu, F., Yu, R., and Guo, M. (2017). Hydrothermal carbonization of forestry residues: influence of reaction temperature on holocellulose-derived hydrochar properties. *J. Mater. Sci.* 52 (3), 1736–1746. doi:10.1007/s10853-016-0465-8
- Luna-Lama, F., Morales, J., and Caballero, A. (2021). Biomass porous carbons derived from banana peel waste as sustainable anodes for lithium-ion batteries. *Materials* 14 (20), 5995. doi:10.3390/ma14205995

Publisher's note

All claims expressed in this article are solely those of the authors and do not necessarily represent those of their affiliated organizations, or those of the publisher, the editors and the reviewers. Any product that may be evaluated in this article, or claim that may be made by its manufacturer, is not guaranteed or endorsed by the publisher.

Supplementary material

The Supplementary Material for this article can be found online at: <https://www.frontiersin.org/articles/10.3389/fenrg.2026.1757714/full#supplementary-material>

- Luna-Lama, F., Caballero, A., and Morales, J. (2022). Synergistic effect between PPy:PSS copolymers and biomass-derived activated carbons: a simple strategy for designing sustainable high-performance Li-S batteries. *Sustain. Energy Fuels* 6 (6), 1568–1586. doi:10.1039/d1se02052h
- Luo, J., Zhang, H., Zhang, Z., Ji, Y., and Yang, Z. (2019). In-Built template synthesis of hierarchical porous carbon microcubes from biomass toward electrochemical energy storage. *Carbon* 155, 1–8. doi:10.1016/j.carbon.2019.08.044
- Major, I., Pin, J.-M., Behazin, E., Rodriguez-Urbe, A., Misra, M., and Mohanty, A. (2018). Graphitization of miscanthus grass biocarbon enhanced by in Situ generated FeCo nanoparticles. *Green Chem.* 20 (10), 2269–2278. doi:10.1039/c7gc03457a
- Marrocchi, A., Cerza, E., Chandrasekaran, S., Sgreccia, E., Kaciulis, S., Vaccaro, L., et al. (2024). Hydrochar from pine needles as a green alternative for catalytic electrodes in energy applications. *Molecules* 29 (14), 3286. doi:10.3390/molecules29143286
- Mihajlović, M., Petrović, J., Maletić, S., Isakovski, M. K., Stojanović, M., Lopičić, Z., et al. (2018). Hydrothermal carbonization of *miscanthus × giganteus*: structural and fuel properties of hydrochars and organic profile with the ecotoxicological assessment of the liquid phase. *Energy Convers. Manag.* 159, 254–263. doi:10.1016/j.enconman.2018.01.003
- Mumme, J., Eckervogt, L., Pielert, J., Diakité, M., Rupp, F., and Kern, J. (2011). Hydrothermal carbonization of anaerobically digested maize silage. *Bioresour. Technology* 102 (19), 9255–9260. doi:10.1016/j.biortech.2011.06.099
- Njoku, V. O., Azharul Islam, M., Asif, M., and Hameed, B. H. (2015). Adsorption of 2,4-Dichlorophenoxyacetic acid by mesoporous activated carbon prepared from H3PO4-Activated langsat empty fruit bunch. *J. Environmental Management* 154, 138–144. doi:10.1016/j.jenvman.2015.02.002
- Qadi, N., Takeno, K., Mosqueda, A., Kobayashi, M., Motoyama, Y., and Yoshikawa, K. (2019). Effect of hydrothermal carbonization conditions on the physicochemical properties and gasification reactivity of energy grass. *Energy Fuels* 33 (7), 6436–6443. doi:10.1021/acs.energyfuels.9b00994
- Randviir, E. P., Omar, K., Liauw, C. M., Miller, G. J., Andrews, H. G., and Smith, G. C. (2019). The physicochemical investigation of hydrothermally reduced textile waste and application within carbon-based electrodes. *RSC Adv.* 9 (20), 11239–11252. doi:10.1039/c9ra00175a
- Rios, S., del Mar, C., Simonin, L., de Geyer, A., Ghimbeu, C. M., and Dupont, C. (2020). Unraveling the properties of biomass-derived hard carbons upon thermal treatment for a practical application in Na-Ion batteries. *Energies* 13 (14), 3513. doi:10.3390/en13143513
- Román, S., Valente Nabais, J. M., Ledesma, B., González, J. F., Laginhas, C., and Titirici, M. M. (2013). Production of low-cost adsorbents with tunable surface chemistry by conjunction of hydrothermal carbonization and activation processes. *Microporous Mesoporous Mater.* 165 (11), 127–133. doi:10.1016/j.micromeso.2012.08.006
- Ru, H., Bai, N., Xiang, K., Zhou, W., Chen, H., and Zhao, X. S. (2016). Porous carbons derived from microalgae with enhanced electrochemical performance for lithium-ion batteries. *Electrochimica Acta* 194, 10–16. doi:10.1016/j.electacta.2016.02.083
- Sagues, W. J., Yang, J., Monroe, N., Han, S. D., Vinzant, T., Yung, M., et al. (2020). A simple method for producing bio-based anode materials for lithium-ion batteries. *Green Chem.* 22 (7), 7093–7108. doi:10.1039/d0gc02286a
- Saha, N., Saba, A., and Toufiq Reza, M. (2019). Effect of hydrothermal carbonization temperature on PH, dissociation constants, and acidic functional groups on hydrochar from cellulose and wood. *J. Anal. Appl. Pyrolysis* 137 (13), 138–145. doi:10.1016/j.jaap.2018.11.018
- Sevilla, M., and Fuertes, A. B. (2009a). The production of carbon materials by hydrothermal carbonization of cellulose. *Carbon* 47 (9), 2281–2289. doi:10.1016/j.carbon.2009.04.026
- Sevilla, M., and Fuertes, A. B. (2009b). Chemical and structural properties of carbonaceous products obtained by hydrothermal carbonization of saccharides. *Chem. Eur. J.* 15 (16), 4195–4203. doi:10.1002/chem.200802097
- Shan, Y. Q., Xu, Z. X., Duan, P. G., Fan, H. L., Hu, X., and Luque, R. (2020). Nitrogen- and sulfur-doped carbon obtained from direct hydrothermal carbonization of cellulose and ammonium sulfate for supercapacitor applications. *ACS Sustain. Chem. Eng.* 8 (42), 15809–15814. doi:10.1021/acssuschemeng.0c05520
- Tian, S., Guan, D., Lu, J., Zhang, Y., Liu, T., Zhao, X., et al. (2020). Synthesis of the electrochemically stable sulfur-doped bamboo charcoal as the anode material of potassium-ion batteries. *J. Power Sources* 448 (36), 227572. doi:10.1016/j.jpowsour.2019.227572
- Unur, E., Brutti, S., Panero, S., and Bruno, S. (2013). Nanoporous carbons from hydrothermally treated biomass as anode materials for lithium ion batteries. *Microporous Mesoporous Mater.* 174, 25–33. doi:10.1016/j.micromeso.2013.02.032
- Wan, H., and Hu, X. (2019). From biomass-derived wastes (Bagasse, wheat straw and shavings) to activated carbon with three-dimensional connected architecture and porous structure for Li-Ion batteries. *Chem. Phys.* 521, 108–114. doi:10.1016/j.chemphys.2019.01.012
- Wang, L., Guo, Y., Zhu, Y., Qu, Y., Rong, C., Ma, X., et al. (2010). A new route for preparation of hydrochars from rice husk. *Bioresour. Technology* 101 (24), 9807–9810. doi:10.1016/j.biortech.2010.07.031
- Wang, L., Schnepf, Z., and Titirici, M. M. (2013). Rice husk-derived carbon anodes for lithium ion batteries. *J. Mater. Chem. A* 1 (17), 5269–5273. doi:10.1039/c3ta10650k
- Wang, H., Yu, W., Shi, J., Mao, N., Chen, S., and Liu, W. (2016). Biomass derived hierarchical porous carbons as high-performance anodes for sodium-ion batteries. *Electrochimica Acta* 188, 103–110. doi:10.1016/j.electacta.2015.12.002
- Wang, K.-T., Jing, C., Wood, C., Nagardeolekar, A., Kohan, N., Dongre, P., et al. (2018). Toward complete utilization of miscanthus in a hot-water extraction-based biorefinery. *Energies* 11 (1), 39. doi:10.3390/en11010039
- Wang, P., Zhu, K., Ye, K., Gong, Z., Liu, R., Cheng, K., et al. (2020a). Three-dimensional biomass derived hard carbon with reconstructed surface as a free-standing anode for sodium-ion batteries. *J. Colloid Interface Science* 561, 203–210. doi:10.1016/j.jcis.2019.11.091
- Wang, Z., Zhang, X., Liu, X., Zhang, Y., Zhao, W., Li, Y., et al. (2020b). High specific surface area bimodal porous carbon derived from biomass reed flowers for high performance lithium-sulfur batteries. *J. Colloid Interface Science* 569, 22–33. doi:10.1016/j.jcis.2020.02.062
- Wang, K., Xu, Y., Wu, H., Yuan, R., Zong, M., Li, Y., et al. (2021). A hybrid lithium storage mechanism of hard carbon enhances its performance as anodes for lithium-ion batteries. *Carbon* 178, 443–450. doi:10.1016/j.carbon.2020.11.095
- Xiong, J., Pan, Q., Zheng, F., Xiong, X., Yang, C., Hu, D., et al. (2018). N/S Co-Doped carbon derived from cotton as high performance anode materials for lithium ion batteries. *Front. Chemistry* 6, 78. doi:10.3389/fchem.2018.00078
- You, X., Misra, M., Gregori, S., and Mohanty, A. K. (2018). Preparation of an electric double layer capacitor (EDLC) using miscanthus-Derived biocarbon. *ACS Sustain. Chem. Eng.* 6 (1), 318–324. doi:10.1021/acssuschemeng.7b02563
- Yu, X., Zhang, K., Tian, N., Qin, A., Liao, L., Du, R., et al. (2015). Biomass carbon derived from sisal fiber as anode material for lithium-ion batteries. *Mater. Lett.* 142 (6), 193–196. doi:10.1016/j.matlet.2014.11.160
- Yu, K., Li, J., Qi, H., and Liang, C. (2018). High-capacity activated carbon anode material for lithium-ion batteries prepared from rice husk by a facile method. *Diam. Relat. Mater.* 86, 139–145. doi:10.1016/j.diamond.2018.04.019
- Yu, K., Wang, J., Song, K., Wang, X., Liang, C., and Dou, Y. (2019). Hydrothermal synthesis of cellulose-derived carbon nanospheres from corn straw as anode materials for lithium ion batteries. *Nanomaterials* 9 (1), 93. doi:10.3390/nano9010093
- Yu, J., Tang, T., Cheng, F., Huang, D., Martin, J. L., Brewer, C. E., et al. (2021). Exploring spent biomass-derived adsorbents as anodes for lithium ion batteries. *Mater. Today Energy* 19, 100580. doi:10.1016/j.mtener.2020.100580
- Yuan, G., Zhang, W., Li, H., Xie, Y., Hu, H., Xiao, Y., et al. (2020). Non-tubular-biomass-derived nitrogen-doped carbon microtubes for ultrahigh-area-capacity lithium-ion batteries. *J. Colloid Interface Science* 580, 638–644. doi:10.1016/j.jcis.2020.07.070
- Zhang, F., Tang, Y., Yang, Y., Zhang, X., and Lee, C.-S. (2016). In-Situ assembly of three-dimensional MoS₂ nanoleaves/carbon nanofiber composites derived from bacterial cellulose as flexible and binder-free anodes for enhanced lithium-ion batteries. *Electrochimica Acta* 211, 404–410. doi:10.1016/j.electacta.2016.05.181
- Zhang, N., Liu, Q., Chen, W., Wan, M., Li, X., Wang, L., et al. (2018). High capacity hard carbon derived from lotus stem as anode for sodium ion batteries. *J. Power Sources* 378, 331–337. doi:10.1016/j.jpowsour.2017.12.054
- Zhang, Y., Zahid, I., Danial, A., Minaret, J., Cao, Y., and Dutta, A. (2021). Hydrothermal carbonization of miscanthus: processing, properties, and synergistic Co-Combustion with lignite. *Energy* 225 (7), 120200. doi:10.1016/j.energy.2021.120200
- Zhao, H., Wang, Q., Deng, Y., Shi, Q., Qian, Y., Wang, B., et al. (2016). Preparation of renewable lignin-derived nitrogen-doped carbon nanospheres as anodes for lithium-ion batteries. *RSC Adv.* 6 (81), 77143–77150. doi:10.1039/C6RA17793J
- Zhao, W., Wen, J., Zhao, Y., Wang, Z., Shi, Y., and Zhao, Y. (2020a). Hierarchically porous carbon derived from biomass reed flowers as highly stable Li-Ion battery anode. *Nanomaterials* 10 (2), 346. doi:10.3390/nano10020346
- Zhao, Y., Shi, J., Wang, X., Li, W., Wu, Y., and Jiang, Z. (2020b). Biomass@MOF-Derived carbon aerogels with a hierarchically structured surface for treating organic pollutants. *Ind. Eng. Chem. Res.* 59 (39), 17529–17536. doi:10.1021/acs.iecr.0c01149
- Zhou, S., Zhou, L., Zhang, Y., Sun, J., Wen, J., and Yuan, Y. (2019). Upgrading earth-abundant biomass into three-dimensional carbon materials for energy and environmental applications. *J. Mater. Chem. A* 7 (9), 4217–4229. doi:10.1039/C8TA12159A
- Zhu, G., Yang, L., Gao, Y., Xu, J., Chen, H., Zhu, Y., et al. (2019). Characterization and pelletization of cotton stalk hydrochar from HTC and combustion kinetics of hydrochar pellets by TGA. *Fuel* 244, 479–491. doi:10.1016/j.fuel.2019.02.039